

Magnetorotational core collapse of possible GRB progenitors. IV. A wider range of progenitors

M. Obergaulinger^{1,2}, M.Á. Aloy^{1,3}

¹ *Departament d'Astronomia i Astrofísica, Universitat de València, C/ Dr. Moliner, 50, 46100 Burjassot, Spain*

² *Institut für Kernphysik, Technische Universität Darmstadt, Schlossgartenstraße 2, 64289 Darmstadt, Germany*

³ *Observatori Astronòmic, Universitat de València, 46980 Paterna, Spain*

5 April 2022

ABSTRACT

The final collapse of the cores of massive stars can lead to a wide variety of outcomes in terms of electromagnetic and kinetic energies, nucleosynthesis, and remnants. The connection of this wide spectrum of explosion and remnant types to the properties of the progenitors remains an open issue. Rotation and magnetic fields in Wolf-Rayet stars of subsolar metallicity may explain extreme events such as superluminous supernovae and gamma-ray bursts powered by proto-magnetars or collapsars. Continuing numerical studies of magnetorotational core collapse including detailed neutrino physics, we focus on progenitors with zero-age main-sequence masses in the range between 5 and 39 solar masses. The pre-collapse stars are one dimensional models employing prescriptions for the effects of rotation and magnetic fields. Eight of the ten stars we consider being the results of chemically homogeneous evolution due to enhanced rotational mixing (Aguilera-Dena et al. 2018). All but one of them produce explosions driven by neutrino heating (more likely for low mass progenitors up to 8 solar masses) and non-spherical flows or by magnetorotational stresses (more frequent above 26 solar masses). In most of them and for the one non-exploding model, ongoing accretion leads to black-hole formation. Rapid rotation makes a subsequent collapsar activity plausible. Models not forming black holes show proto-magnetar driven jets. Conditions for the formation of nickel are more favourable in magneto-rotationally driven models, though our rough estimates fall short of the requirements for extremely bright events if these are powered by radioactive decay. However, approximate light curves of our models suggest that a proto-magnetar or black hole spin-down may fuel luminous transients (with peak luminosities $\sim 10^{43\text{--}44}$ erg).

Key words: Supernovae: general - gamma-ray bursts: general - stars: neutron - stars: black holes - (*magnetohydrodynamics*) MHD

1 INTRODUCTION

The core collapse of a star with more than $\sim 8 M_{\odot}$ after the end of its hydrostatic burning phases initiates a sequence of processes leading to one of several quite different outcomes. The star may explode as a core-collapse supernova (CCSN) or not explode at all, while the long-term central compact remnant can either be a black hole (BH) or a neutron star (NS). Furthermore, in special cases, the dynamics of the compact remnant may produce suitable conditions for an even more luminous high-energy transient, namely a long gamma-ray burst (GRB). These explosions are ultimately powered by the gravitational binding energy liberated during the collapse and the subsequent accretion of matter onto the core. While this energy source is universal, there are different mechanisms for converting a fraction of it to the

kinetic and internal energy of the ejecta of the explosion. Hence, the evolution depends on the pre-collapse state of the progenitor star and on a multitude of complex, interconnected processes occurring during and after the collapse and the birth of a proto-neutron star (PNS).

The detection of neutrinos from supernova SN 1987A, a large number of increasingly detailed multi-dimensional simulations, and the comparison of their results to electromagnetic observations of CCSNe and young supernova remnants (SNRs) offer confirmation for the standard neutrino-driven mechanism (for a review, see Janka 2012). This scenario, based on neutrinos depositing energy and on non-radial fluid instabilities in the hot bubble surrounding the PNS, is able to explain the bulk of the observed CCSNe without requiring special conditions for the progenitor.

However, it remains difficult to account for the most

extreme events such as hypernovae (HNe; Iwamoto et al. 1998), i.e., the most energetic class of CCSNe, or long GRBs characterized by collimated, relativistic outflows. Since these events constitute only a minor fraction of the entire population, they have been connected to special progenitor classes, in particular stars with high rotation rates. In these cases, magnetic fields may play a crucial role in launching the explosion by tapping into the rotational energy. Additionally, rotation and magnetic fields have been invoked to explain the extraordinary brightness of super-luminous supernovae (SLSNe; e.g. Gal-Yam 2012; Moriya et al. 2018; Gal-Yam 2019; Inserra 2019).

The basic building blocks of magnetorotational models are either a fast spinning, strongly magnetized PNS, a so-called proto-magnetar (PM; Kasen & Bildsten (2010) -KB10 hereafter-; Woosley (2010); Metzger et al. (2011); Nicholl et al. (2017)), whose spin-down drives the explosion (HNe or GRBs) or heats the ejecta (SLSNe), or accretion of rapidly rotating matter onto a BH magnetically powering relativistic jets (collapsar model for GRBs; MacFadyen et al. 2001; Obergaulinger & Aloy 2017).

Whether the strong magnetic fields required for these types of explosions can be reached depends on various processes amplifying them in the collapsed core and on the pre-collapse configuration. Therefore, models for this class of explosions should be based on progenitor stars that include the effects of rotation and magnetic fields in a self-consistent manner. However, the computational costs for covering the entire pre-collapse life of a star up to collapse restrict stellar evolution calculations to the assumption of spherical symmetry, thus allowing for an inclusion of these effects only in approximate ways. Among the most advanced such approximations is the model for a dynamo in convectively stable layers of stars proposed by Spruit (2002) which has been incorporated into spherically symmetric stellar evolution models to produce pre-collapse models (e.g., Heger et al. 2005). Woosley & Heger (2006) presented a set of potential progenitors for GRBs that have found wide application in numerical investigations of stellar core collapse and its aftermath. Among those studies, we refer to the previous articles in this series (Obergaulinger & Aloy 2020; Aloy & Obergaulinger 2021; Obergaulinger & Aloy 2021, Paper I; Paper II; Paper III, hereafter) evolving various variations of two progenitors in axisymmetry as well as three dimensions including all the physics relevant during the formation of the PNS and the subsequent evolution until explosion (or lack thereof). We note that many other works took a different approach and simulated the propagation of relativistic jets in progenitors of this group under the assumption that the cores develop the conditions necessary for producing a GRB (for an overview, see, e.g., Corsi & Lazzati 2021).

More recently, Aguilera-Dena et al. (2018) (AD18) as well as Aguilera-Dena et al. (2020) have produced a sequence of rotating, magnetized pre-collapse models for Wolf-Rayet stars marked by strong stellar winds. The resulting loss of the outer layers is, besides rotation and magnetic fields, another important ingredient in models for the aforementioned extreme explosions. It is, however, accompanied by a loss of angular momentum, which might reduce the prospects of retaining enough rotational energy for such an explosion. Nevertheless, these stars undergo a chemically homogeneous evolution (CHE) due to an adjustment of the mixing of gas

between different layers induced by rotation and end their lives with high angular velocities. AD18 used an approximation to predict the possible outcome of the core collapse of their models, finding several candidates for SLSNe and for GRBs driven by PMs and collapsars.

As the studies on magnetorotational core collapse summarized above indicate, the models of AD18 in principle possess the right properties to produce SLSNe and GRBs. Thus, a closer investigation by self-consistent simulations of the collapse and the subsequent phases is needed, and this is the motivation of this paper. We complement the set of CHE models with model 16TI from Woosley & Heger (2006). This star has an initial mass of $M_{ZAMS} = 16 M_{\odot}$ and sub-solar metallicity ($Z = 0.1 Z_{\odot}$). 16TI is a plausible collapsar-forming progenitor due to its structure and in particular its fast rotation. It has been used in several studies of the propagation of jets launched by an BH-accretion-disc system through the stellar envelope. However, previous work (e.g., Lazzati et al. 2009; Lazzati et al. 2012; Hayakawa & Maeda 2018; Aloy et al. 2018), assumes that the core has formed such a BH-accretion-disc structure. The central regions, including the BH-torus system or any other type of compact remnant, are excised and a jet injected through a suitably chosen inner boundary is evolved in the framework of relativistic (magneto-)hydrodynamics. By simulating the phase prior to that stage, we complement these studies and explore the possibility of this star actually satisfying the conditions for launching a collapsar jet in the first place.

We combine magnetohydrodynamics (MHD) and a two-moment neutrino transport to follow the evolution of eight CHE progenitor models between 5 and $39 M_{\odot}$, along with model 16TI. Our goal is to check the predictions regarding the evolution of the stars. To this end, long simulation times and a large number of models are required. For this reason, we restrict ourselves at this point to two-dimensional models and defer detailed three-dimensional models to a later stage.

This article is organized as follows: Sect. 2 briefly introduces the physics included in the simulations and the numerical methods, Sect. 3 summarizes the progenitor models selected in this study, Sect. 4 presents the simulation results, Sect. 5 roughly estimates the observable signal of the models, and Sect. 6 ends the article with concluding remarks.

2 INPUT PHYSICS AND NUMERICS

Methodologically, the present study follows our previous work on stellar core collapse (Obergaulinger et al. (2014); Obergaulinger & Aloy (2017); Paper I). We employed the simulation code Alcar (Just et al. 2015) for solving the combined systems of equations of special relativistic MHD equations and spectral two-moment neutrino transport. The gas is described by the SFHo equation of state (EOS) of Steiner et al. (2013) applied at densities $\rho > \rho_{EOS} = 6000 \text{ g cm}^{-3}$ and an EOS accounting for a mixture of photons, electrons and positrons, and nucleons below this threshold. The nuclear composition is determined from nuclear statistical equilibrium (NSE) and using the flashing scheme of Rampp & Janka (2002) in the high-density and low-density regimes, respectively. The self-gravity of the gas is modelled by version 'A' of the TOV potential of Marek et al. (2006), which yields a very close approximation to general relativity in

terms of, e.g., the evolution of the density profiles of PNSs and the maximum mass of stable cold neutron stars.

We evolve neutrinos in the two-moment transport scheme consisting of a set of balance equations for their energy (0th moment) and momentum (1st moment) densities closed by a local algebraic expression for the pressure tensor (2nd moment). One pair of these equations is solved for each neutrino species (electron neutrinos, electron anti-neutrinos, and heavy-lepton neutrinos) and for each one of several bins in the space of neutrino energies. The energy bins are coupled by velocity-dependent and gravitational terms in the $\mathcal{O}(v/c)$ -plus method of Endeve et al. (2012). Neutrinos and matter interact via the most important reactions: nucleonic and nuclear absorption, emission, and scattering, inelastic scattering off electrons, and the pair processes of electron-positron annihilation and nucleonic bremsstrahlung.

The simulations are run in spherical coordinates assuming axisymmetry. We set up grids with $n_r = 480$ radial zones distributed logarithmically up to an outer radius of $R_{\text{out}} = 7 \times 10^{10}$ cm and $n_\theta = 128$ zones in angle. In energy, a logarithmic grid of $n_\epsilon = 10$ bins with a maximum energy of $\epsilon_{\text{max}} = 240$ MeV is used.

3 INITIAL MODELS

Our set of models includes a progenitor employed in our previous studies, viz. a star of an initial mass of $M_{\text{ZAMS}} = 35 M_\odot$ and sub-solar metallicity ($Z = 0.1 Z_\odot$) evolved to the pre-collapse stage with rotation and magnetic fields by Woosley & Heger (2006). Among the different versions of the models based on the progenitor 350C, we only use the one with profiles of rotation and magnetic field taken from the stellar evolution calculations as a comparison model here. The model was named 350C-R0 in the previous articles of this series; for the sake of brevity, we refer to it as model 350C in the following.

All the other initial conditions of our simulations are given by eight stellar models computed by AD18. These are models for rapidly rotating Wolf-Rayet stars with magnetic fields at subsolar metallicity of $Z = 0.02 Z_\odot$ evolved in spherical symmetry using the Modules for Experiments in Stellar Astrophysics (MESA) code (Paxton et al. 2011, 2013, 2015, 2018). The magnetic fields are evolved following the Taylor-Spruit dynamo (Heger et al. 2005), i.e., the treatment of magnetic fields through the stellar evolution is effectively the same as in models 350C and 16TI. The stars are set up with an angular velocity rate close to the critical rotation rate. The fast rotation leads to efficient mixing across different layers of the star. Thereby, these models undergo a chemically homogeneous evolution (CHE). AD18 computed two sets of models, one with the standard sets of parameters and another one with an increased rate of rotational mixing (series B). It is from the latter that we select our pre-collapse models.

At the end of their hydrostatic evolution, the stars of series B have lost their H envelope and most of the He layer. They retain a large amount of angular momentum and possess magnetic fields whose strength depends on the specific progenitor. These properties make them possible progenitors for type Ic SLSNe or GRBs. AD18 explored the types of explosions to be expected as follows:

- The stars with lowest initial masses ($M_{\text{ZAMS}} = 5, 8,$ and $13 M_\odot$) may explode as type Ic SLSNe in which the excess luminosities are caused mostly by energy input from a central PM.
- The stars with higher masses fulfil the expectations for forming a GRB, in particular in terms of the angular momentum in the core. AD18 suggest that the ones in an intermediate mass range (models with 17 and $20 M_\odot$) might avoid BH formation and thus yield to PM-powered GRBs.
- More massive stars (in our sample, the ones with 26, 30, and $39 M_\odot$) might end their lives as collapsars.
- Though we do not include them in our sample, we note for the sake of completeness that AD18 also consider more massive stars that might, after undergoing pulsational pair instability, explode as GRBs or HNe and, by interaction with the stellar winds evolve into SLSNe.

In the process of mapping the stellar models at the onset of collapse onto our 2d grid, we have to convert the radial profiles of the poloidal and toroidal field components into the three vector components of the magnetic field, (b^r, b^θ, b^ϕ) , as a function of radius and latitude. Proceeding in the same way as in Obergaulinger & Aloy (2017, 2020), we assume a large-scale geometry of the field restricted to the layers of the star which are magnetized. The radial and lateral components, on the one hand, and the azimuthal components, on the other hand, are respectively computed from the poloidal and the toroidal components of the stellar evolution model, all of them modulated by a factor $\sin \theta$. We note that, since the Taylor-Spruit dynamo is designed for radiative layers of stars, the magnetic field vanishes in convective layers by construction.

We present the structure of the progenitors at the onset of collapse in Fig. 1 and Fig. 2. In the former figure, the *top panel* displays the density profiles of the stars, the *mid panel* with profiles of the specific entropy gives an overview of the location of shell interfaces in the cores, and the *bottom panel* shows the compactness parameter (O'Connor & Ott 2011),

$$\xi(m) = (m/M_\odot) (1000 \text{ km}/r(m)), \quad (1)$$

defined by the mass m enclosed in a radius $r(m)$. The latter figure compares the profiles of specific angular momentum in the equatorial planes of the progenitors to the specific angular momentum of the last stable orbits for gas at a Lagrangian coordinate m orbiting black holes that would form from the collapse of all the matter inside of it. For those comparison profiles, we assume non-rotating and maximally rotating BHs as well as BHs whose angular momentum is equal to that of all the layers up to the mass coordinate m . Shells whose actual specific angular momentum exceeds the ones of the last stable orbits can be expected to form discs around BHs rather than directly fall into them (the mass coordinate where this happens is marked with a blue asterisk). The fact that in all models of Fig. 2 matter above a finite mass coordinate can form an accretion disc indicates that in all of them a collapsar could form if a the compact remnant left after core collapse becomes a BH. Should the post-collapse PNS become a NS in the long term, the high specific angular momentum of these layers may limit the amount of mass that can be accreted over the central object. Furthermore, layers of the stars with non-vanishing magnetic fields are shaded in these panels.

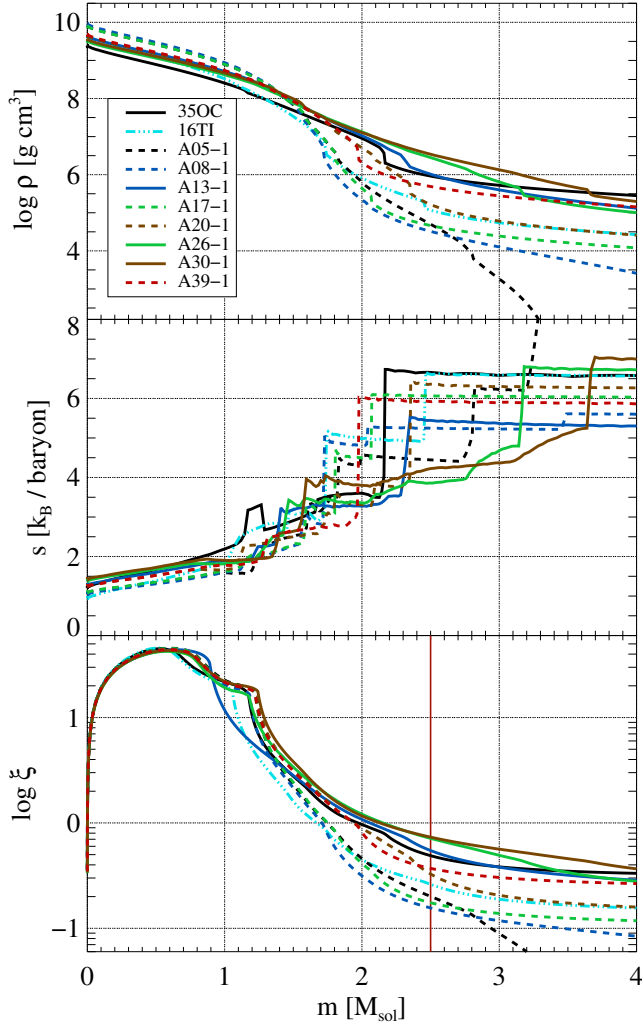


Figure 1. Top to bottom: profiles of density, specific entropy, and compactness of all progenitors at the onset of collapse. Models producing neutrino-driven explosions, MHD effects or fail to explode are displayed with dashed, solid and dash-dotted lines, respectively. The vertical line in the bottom panel marks the mass coordinate $m = 2.5M_{\odot}$, facilitating the comparison of the values of ξ at that mass coordinate for each model. Here, the compactness ξ is not evaluated at the time of bounce as it is the case of $\xi_{2.5}$ in Tab. 1.

4 RESULTS

4.1 Overview

We summarize the outcomes of our simulations in Tab. 1, listing the explosion mechanism and the kind of compact remnant in comparison to the predictions of AD18 for the evolution of the stars where applicable. Model 16TI fails to launch an explosion during the entire time simulated and will produce a BH within a few more seconds. All other models experience delayed shock revival initiated by a combination of neutrino heating, non-spherical fluid flows, and magnetorotational stresses. The importance of these effects as well as the time of explosion vary greatly across the mass range. In some cases, the explosion is sufficiently strong to quench accretion onto the PNS and prevent BH forma-

tion, but most cores, in particular at higher stellar masses ($M_{\text{ZAMS}} \geq 20M_{\odot}$), are likely to end up as BHs.

In the following, we will describe the most important features characterizing the evolution of several groups of models:

- (i) neutrino-driven explosions leading to NS or BH formation: models A05, A08, A17, A20, A39;
- (ii) MHD explosions with BH formation: models A13, A26, A30, 350C;
- (iii) the failed explosion of model 16TI.

4.2 Neutrino-driven explosions

We will focus our discussion on models whose explosion is chiefly driven by neutrinos. Neutrino-driven explosions require (at least) that the heating time scale due to neutrinos be comparable or larger than the advection timescale through the gain layer. Models A05, A08, A17, and A20 undergo shock revival with a delay after core bounce between $t_{\text{exp}} \approx 1.0$ s (A20) and $t_{\text{exp}} \approx 3.2$ s (A08) (see evolution of the maximum shock radius in *top panel* of Fig. 3). Model A39 explodes much earlier ($t_{\text{exp}} \approx 0.5$ s) and, showing a more pronounced influence of the magnetic field, could be considered an intermediate case between this class and that of MHD explosions (Sec. 4.3).

After the onset of the explosion, the shock wave expands at high speeds and the diagnostic explosion energies and ejecta masses (Fig. 3 *mid and bottom panels*) rise. By the end of the simulations, the explosion energies are around $E_{\text{ej}} \approx 5 \times 10^{50}$ erg s $^{-1}$ carried by $M_{\text{ej}} \approx 0.1 \dots 0.4 M_{\odot}$ of unbound gas. Both quantities keep increasing throughout the final phases of the simulation. Model A17 is an exception in that it shows a very rapid rise of E_{ej} by almost 10^{51} erg within about 0.5 s (starting at a post-bounce time $t_{\text{pb}} \approx 3.1$ s) without a similar growth of M_{ej} . This quick rise, which does not show any sign of levelling off, corresponds to the activation of a wind powered by the magnetic spin-down of the PNS, which by then has turned into a PM due to a growth of the surface field strength. This late-time evolution does not interfere with the revival of the SN shock wave.

Due to the large rotational energy existing in the stellar progenitors of all the models in this study, the compact remnant left by their core collapse stores a rather large rotational energy, \mathcal{T}_{PNS} (Tab. 1). Thus, even neutrino-driven explosion models harbor an additional source of energy that can be transferred to the ejecta. It is, nevertheless, arguable whether this extra energy will be a sizeable fraction of \mathcal{T}_{PNS} or only the (significantly smaller) free rotational energy of the PNS, \mathcal{F}_{PNS} (defined in Eq. (5) below).

The models of this group tend to possess the least compact cores among the progenitors considered here. Their density profiles, $\rho(m)$ (Fig. 1 *top panel*; dashed lines), exhibit a strong decrease at mass coordinates $m < 2M_{\odot}$ near the location of the surface of the inner core, which show up as discontinuities in the specific entropy and the electron fraction (Fig. 1 *middle panel*). The comparably low densities further out correspond to moderate values of the compactness parameter, $\xi_{2.5}$, computed at $m = 2.5M_{\odot}$ according to Eq. (1), are listed in Tab. 1 (see also Fig. 1, *bottom panel*). These values are significantly below the threshold $\xi_{2.5} \approx 0.45$ of explodability (O’Connor & Ott 2011) and,

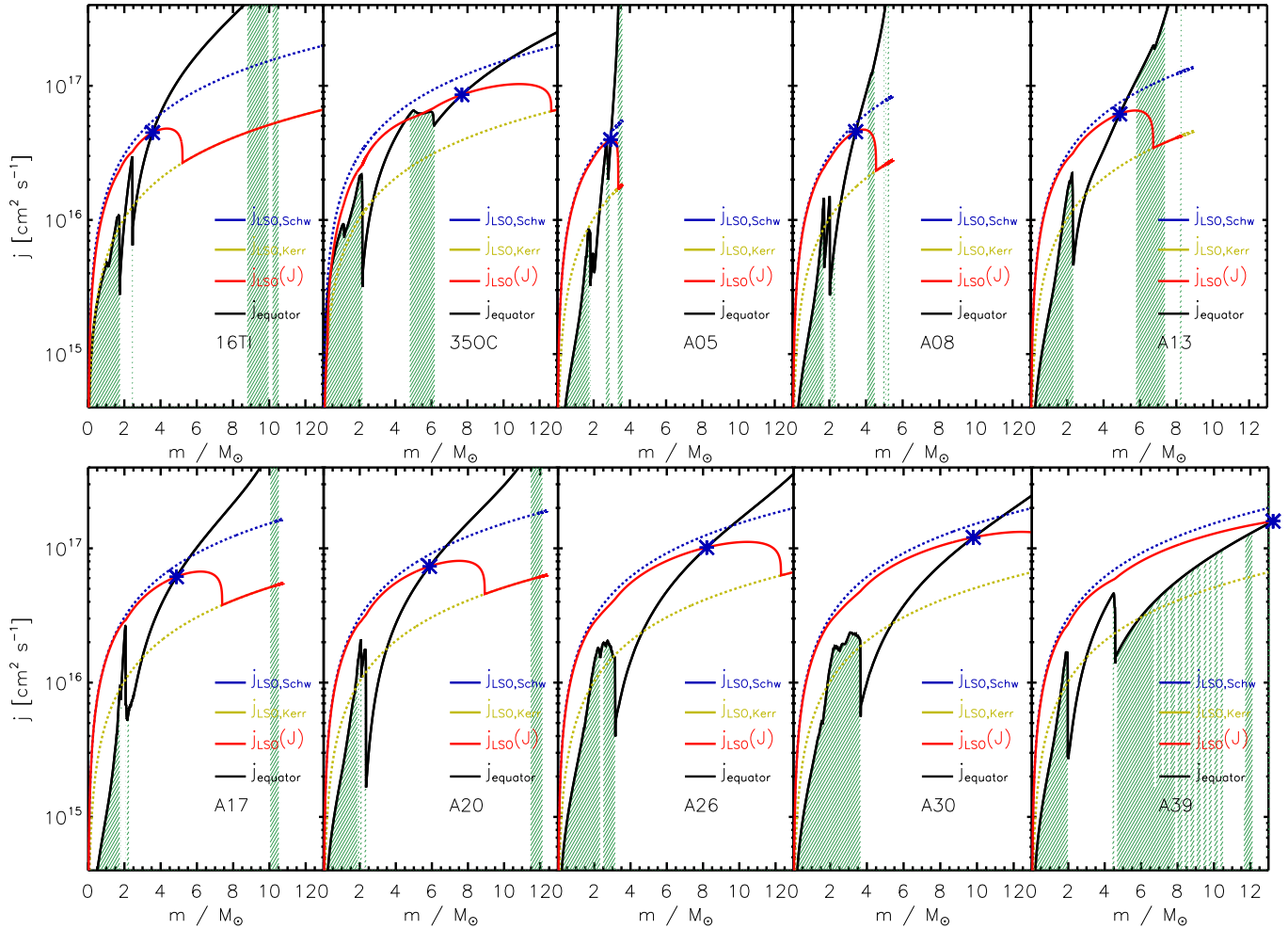


Figure 2. Equatorial profile of the initial specific angular momentum (black lines) of models as indicated in the panels. In each panel, the blue dashed lines denote the angular momentum needed to support matter at the LSO for a Schwarzschild BH, while the yellow dashed lines are for a Kerr BH with dimensionless spin $a = 1$. The red lines indicate the specific angular momentum at the LSO for a BH with the mass and angular momentum inside the displayed mass coordinate in the pre-SN star. The green-hatched parts of the plot denote the mass shells of the pre-SN star with non-zero magnetic field.

hence, these stellar models should easily yield successful supernova explosions. During the pre-explosion phase, these models develop low mass accretion rates through the stalled shock due to the low densities beyond the densest central part of the star (Fig. 3, *top panel*). Ertl et al. (2016) defined a two-parameter criterion for classifying the explodability of massive stars by the neutrino-driven mechanism of *non-rotating* models. These two parameters are M_4 , defining the normalized enclosed mass for a dimensionless entropy per nucleon of $s = 4$,

$$M_4 \equiv m(s=4)/M_\odot \quad (2)$$

and μ_4 , the normalized mass derivative at this location

$$\mu_4 \equiv |(dm/M_\odot)/(dr/1000 \text{ km})|_{s=4} \quad (3)$$

According to Ertl et al. (2016), the parameters μ_4 and $\mu_4 M_4$ tightly correlate with the neutrino luminosity and the mass accretion rate through the stalled shock, respectively. Our neutrino-driven explosion models, possess the smallest values of M_4 , of μ_4 , and of $\mu_4 M_4$ of all the sample (Tab. 1). Although our models are fast rotators, we also notice that

small values of μ_4 correlate with the small neutrino luminosities (Fig. 4, *upper panel*). Likewise, the small values of the product $\mu_4 M_4$, correlate with the mass accretion rate onto the PNS (or through the shock; Fig. 3 *bottom panel*). Figure 5 represents the models of Tab. 1 in the $\mu_4 M_4 - \mu_4$ plane. The black line represents an approximate division of the plane in BH forming and NS forming models according to Ertl et al. (2016). Specifically, the line that we represent is $y = k_1 x + k_2$, where $y = \mu_4 M_4$, $x = \mu_4$, and the coefficients $k_1 = 0.283$ and $k_2 = 0.043$ are taken from one of the sets of fits of Ertl et al. (2016). We observe that not only BH forming models lie above the division line, but also some models, and may hardly form an NS in a longer timescale than spanned by our calculations. Furthermore, below the division line there are models which will likely form NS later on (as expected according to the classification of Ertl et al. 2016) as well as a BH forming case, precisely that of model A20, which produces a neutrino-driven explosion. Using other values for k_1 and k_2 , the two-parameter classification criterion does not improve much (we have used all the possible combinations of k_1 and k_2 from Table 2 of Ertl

model	AD18	M_4	μ_4	$\mu_4 M_4$	\mathcal{T}_4	$\lambda_{2.5}$	$\overline{B}_{2.5}^p$ [10^{10} G]	$\overline{B}_{2.5}^t$ [10^{10} G]	$\xi_{2.5}$	t_f [s]	t_{exp} [s]	$M_{\text{sh,e}}$ [M_\odot]	kind	E_{exp}	\mathcal{F}_{PNS} [10^{51} erg]	\mathcal{T}_{PNS}	remn.	M_{r}	M_{Ni} [M_\odot]
35OC	--	2.15	0.20	0.43	8.61	0.58	250	54.8	0.49	2.6	0.19	1.9	ν /M	1.2	5.5	148.5	BH	2.9	0.048
16TI	--	1.73	0.14	0.25	2.9	0.13	24.5	17.7	0.26	6.1	--	--	--	--	1.1	128.7	BH	2.8	--
A05	SLSN	1.82	0.11	0.21	0.70	0.05	0.70	1.26	0.20	3.7	1.7	2.1	ν	1.9	0.40	10.64	PNS	2.2	0.011
A08	SLSN	1.72	0.09	0.16	1.4	0.06	0.89	0.55	0.16	4.8	3.4	2.1	ν	0.43	0.54	18.11	PNS	2.2	0.003
A13	SLSN	2.30	0.19	0.44	2.5	0.69	8.26	4.15	0.55	2.9	0.39	2.2	M	0.76	0.09	45.74	BH	2.6	0.050
A17	PM	2.07	0.05	0.11	0.76	0.05	1.42	0.36	0.17	3.9	1.7	2.1	ν	1.1	2.2	17.45	PNS	2.1	0.009
A20	PM	2.34	0.08	0.18	2.2	0.09	0.57	0.91	0.32	4.0	1.2	2.4	ν	0.49	2.7	53.58	BH	2.5	0.011
A26	Col	2.76	0.21	0.58	2.9	0.74	3.64	2.53	0.71	1.5	0.56	2.5	M	0.98	1.5	83.49	BH	3.0	0.022
A30	Col	2.28	0.33	0.75	2.1	0.98	6.85	3.72	0.73	1.5	0.39	2.3	M	1.4	2.8	89.74	BH	3.0	0.036
A39	Col	1.97	0.12	0.25	2.6	0.33	8.87	4.31	0.37	3.8	0.51	2.1	ν /M	0.56	5.8	41.20	BH	2.4	0.030

Table 1. Overview of models: model name, evolution according to AD18 (superluminous SN, PM with the potential to produce a GRB, or collapsar -denoted with “Col”-), properties of the stellar progenitor at the presupernova link, M_4 (Eq. (2)), μ_4 (Eq. (3)), $\lambda_{2.5}$ (Eq. (4)) \mathcal{T}_4 (the rotational energy of the matter inside M_4 in units of [10^{48} erg]), and volume-averaged poloidal and toroidal magnetic field strength within the inner $2.5M_\odot$. The compactness parameter $\xi_{2.5} := \xi(2.5M_\odot)$ (Eq. (1)) is measured at the time of bounce. The rest of the columns are: final and explosion times in seconds after bounce, the mass inside the shock wave at the onset of explosion ($M_{\text{sh,e}}$), the kind of explosion (neutrino driven, ν ; magnetorotational, M), the final explosion energy, E_{exp} , the free energy of the rotation of the PNS, \mathcal{F}_{PNS} , and the rotational energy of the PNS, \mathcal{T}_{PNS} , at the end of the simulation, the type of remnant (the acronym BH is set in boldface if BH formation occurs during the simulation; in this case, the final simulation time is the BH formation time) and its mass at the final time, M_{r} , and an estimate for the expelled mass of Ni, M_{Ni} .

et al. 2016). For the set of models at hand, values $k_1 \sim 0$, $k_2 \sim 0.12$ yield a better classification between BH forming and NS forming models. Nevertheless, the parameters $\xi_{2.5}$, M_4 , and μ_4 do not gather direct information about the rotational and magnetic properties of the stellar progenitor. Hence, they (or their combinations) may only be approximately used to predict whether an explosion will be neutrino-driven or magneto-rotational. We have explored a number of additional indicators for that end.

First, we have searched for the existence of simple correlations between the rotational energy of the progenitor, the explosion type, and the compact remnant. Precisely, we compute the rotational energy inside $m = M_4$, measured in units of 10^{48} erg, \mathcal{T}_4 . This quantity does not discriminate between exploding or non-exploding models. For instance, model 16TI, which fails to explode, has a similar value of \mathcal{T}_4 as model A26, which explodes magneto-rotationally. There is, however, a broad correlation between the explosion type and the value of \mathcal{T}_4 . Larger values of $\mathcal{T}_4 \gtrsim 2.1$ yield magneto-rotational or mixed type explosions (where magneto-rotational effects act together with neutrinos). Conversely, values $\mathcal{T}_4 \lesssim 2.1$ associate with neutrino-driven explosions. The compact remnant type also correlates with \mathcal{T}_4 . Small values of $\mathcal{T}_4 (\lesssim 1.4)$ yield PNSs as compact remnants, while large values of $\mathcal{T}_4 (\gtrsim 1.4)$ produce BHs (Tab. 1). We add a cautionary note here. The final fate of the compact remnant is (to some extent) sensitive to the dimensionality of the model. Models in 3D display a significantly smaller mass growth rate of the PNS after $t_{\text{pb}} \sim 0.2$ s (Paper II; Paper III). Hence, BH formation (if at all happens) may take some more time in 3D than in 2D.

Second, we stress the fact that the structure of the star is formed by a set of magnetized layers intertwined with non-magnetized ones. We may compute the average coherence length of the poloidal magnetic field within the inner $2.5M_\odot$

as

$$\bar{l}_{\text{pol}} \equiv \frac{1}{N_{\text{layers}}} \sum_{i=1}^{N_{\text{layers}}} \Delta_i,$$

where Δ_i is the radial width of a magnetized layer and N_{layers} is the number of magnetized layers up to a mass coordinate $m = 2.5M_\odot$. The choice of the mass coordinate $m = 2.5M_\odot$ is arbitrary, but we have checked that the results that follow do not sensitively depend on the exact mass considered. Since it is customary to evaluate the compactness ratio at $m = 2.5M_\odot$, we have adopted this value. We note that, e.g., in most cases $M_4 \lesssim 2.5M_\odot$. Evaluation of the coherence length until $m = M_4$ yields qualitatively similar results.

If we denote $r_{2.5}$ the radius corresponding to $m = 2.5M_\odot$, we can build the following dimensionless ratio

$$\lambda_{2.5} \equiv \bar{l}_{\text{pol}}/r_{2.5} \quad (4)$$

Values of $\lambda_{2.5}$ close to 1 mean that the inner core of the star is all magnetized and that the magnetic field connects stellar matter from the centre to $r_{2.5}$. In Paper II we stressed the fact that a larger poloidal magnetic field coherence length helps develop magnetorotational explosions. This is because after bounce, the PNS is magnetically connected to the gain region and may transfer angular momentum and energy there by magneto-centrifugal effects. In Tab. 1 we observe the clear correlation between $\lambda_{2.5}$ and the kind of explosion. If $\lambda_{2.5} \gtrsim 0.3$, magnetic effects are important for the explosion success, while if $\lambda_{2.5} < 0.1$ neutrinos are the main driver for the explosion. It is significant that the magnetic field strength within the inner region of the progenitor star does not clearly correlate shows some correlation with the explosion mechanism. We support this statement computing the volume-averaged poloidal (toroidal) magnetic field strength in the region interior to $m = 2.5M_\odot$, $\overline{B}_{2.5}^p$ ($\overline{B}_{2.5}^t$; see Tab. 1). Models with $\overline{B}_{2.5}^p \lesssim 1.3 \times 10^{10}$ G develop neutrino-driven explosions. However, possessing a large volume-averaged magnetic field strength does not guarantee that neutrinos do

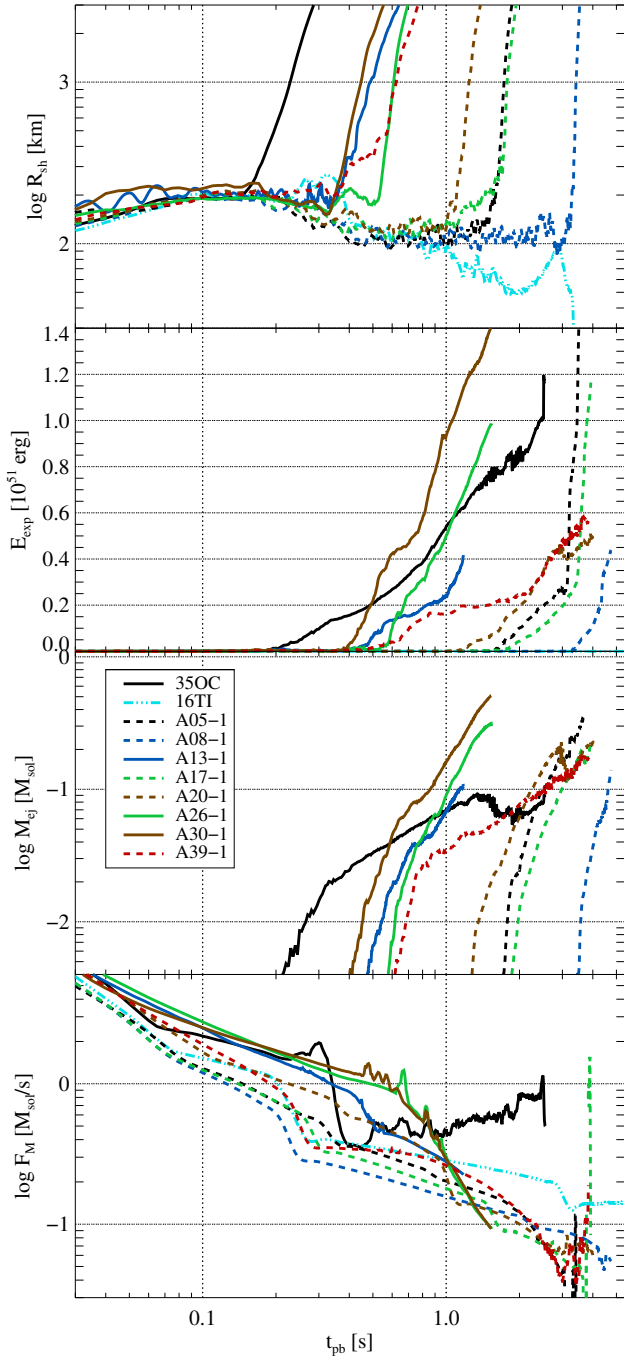


Figure 3. Top to bottom: shock radius, explosion energy, ejecta mass, and mass flux through the shock wave as functions of post-bounce, t_{pb} .

not play any role in the explosion. This is the case, e.g., in model A39, which yields a mixed-type explosion although it has a volume-averaged magnetic field very similar to that of model A17, which is one of the clearest examples of magneto-rotationally driven-explosion. CHE models show poloidal and toroidal fields $\sim 1 - 2$ orders of magnitude smaller than non-CHE models. This fact does not prevent that some CHE models develop magneto-rotational explosions. As in

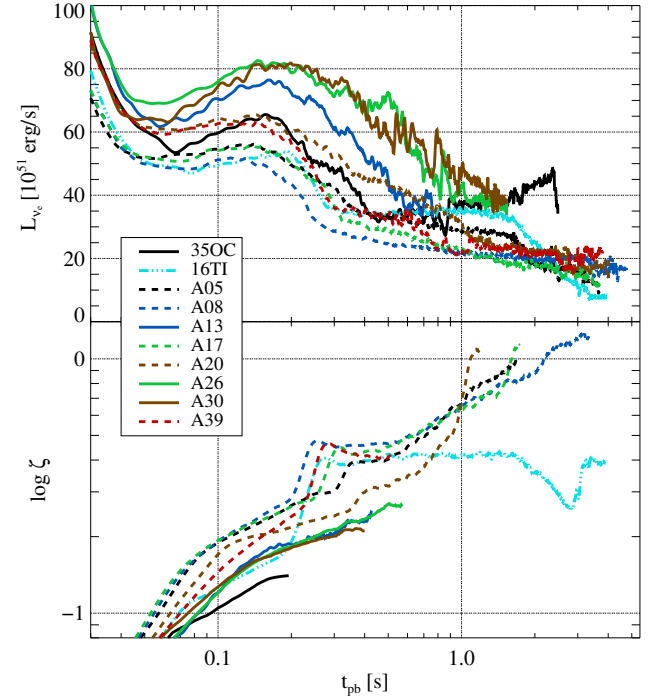


Figure 4. Top panel: luminosities of electron neutrinos. Bottom panel: ratio of the total neutrino luminosity to the mass accretion rate through the shock, ζ .

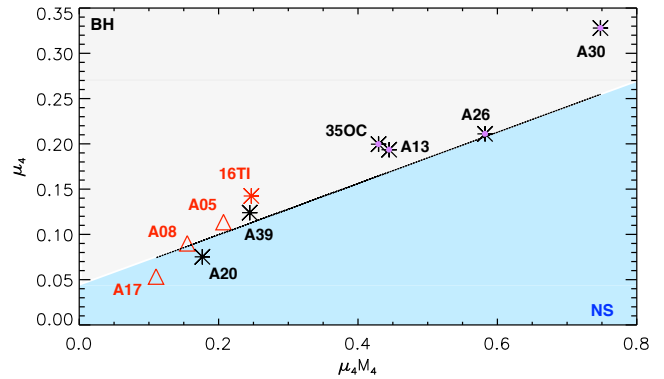


Figure 5. Representation of the computed models in the $\mu_4 M_4 - \mu_4$ plane. The black line corresponds to $y = 0.283x + 0.043$, where $y = \mu_4$ and $x = \mu_4 M_4$. Black asterisks identify models of Tab. 1 that yield BHs, while red triangles correspond to models that do not form BHs. The red asterisk represents model 16TI, which has not formed a BH by the end of the computed time. Asterisks with an overlaid magenta circle correspond to models that develop early magneto-rotational explosions.

the case of the quantity \mathcal{T}_4 , $\lambda_{2.5}$ does not allow predicting whether a specific model may or may not explode.

Despite the favourable conditions for explosions, it takes more than one second to achieve shock revival. Relative to the models exploding earlier due to MHD effects, these cores tend to emit neutrinos at lower total luminosities (see Fig. 4, upper panel). The luminosities are not only lower in absolute values, but also relative to the gravitational energy of the PNSs. While, the production of neutrinos seems less efficient in this group of models, their effect on the dynamics is

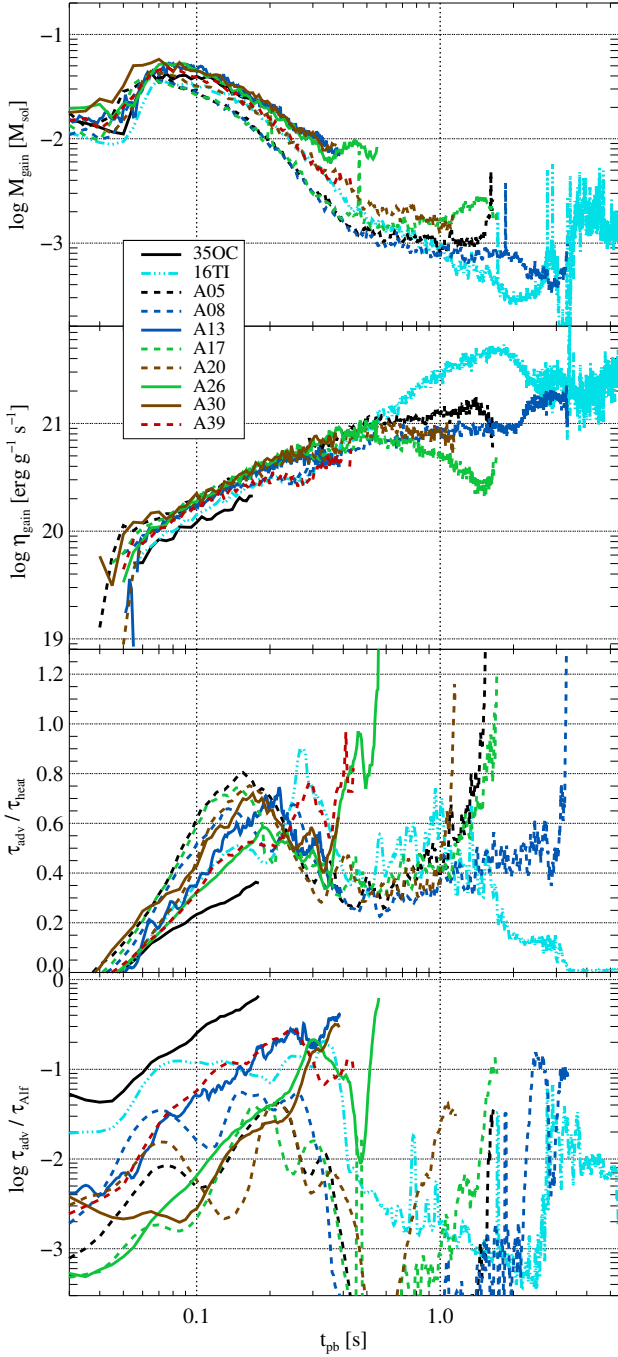


Figure 6. Top to bottom: mass in the gain layer, heating efficiency, ratio between advection and heating timescales, and between the advection and the Alfvén timescales. The lines and their colors are as in Fig. 4. The evolution is only displayed until the definitive shock expansion sets in.

higher. We can quantify this effect with the ratio of the total neutrino luminosity to the mass accretion rate through the shock, $\zeta = L_\nu / (\dot{M}c^2)$ (*bottom panel*). Throughout the entire runs, models A05, A08, A17, A20, and A39 show higher values of ζ than models exploding magnetorotationally. Their shock revival sets in when at $\zeta \gtrsim 1$. At that time, the mass in the gain layer has decreased to a few $10^{-3} M_\odot$ (Fig. 6, *top*

panel), while the heating efficiency, $\eta_{\text{gain}} = Q_{\nu, \text{gain}} / M_{\text{gain}}$, rises until the explosion sets in (Fig. 6, *second panel*). The neutrino heating timescale in the gain layer, τ_{heat} , is considerably longer than the advection timescale, τ_{adv} , except for an episode around $t_{\text{pb}} \approx 0.1 \dots 0.2$ s. The average of the ratio $\tau_{\text{adv}} / \tau_{\text{heat}}$ over the gain layer (Fig. 6 *third panel*) rapidly rises above unity, but only immediately before the shock wave revives. We note that, compared to model 350C, all new models come closer to fulfilling the explosion criterion of $\tau_{\text{adv}} / \tau_{\text{heat}} = 1$ during an earlier phase of their evolution ($t_{\text{pb}} = 0.1 \dots 0.2$ s). The heating rate, however, does not suffice to increase the total energy of the gain layer to positive values. The failure can in part be attributed to a relatively low activity of non-spherical flows during this time. Furthermore, the magnetic energies in the gain layer are low and correspond to ratios between the advection time and the Alfvén travel time across the gain layer, $\tau_{\text{adv}} / \tau_{\text{Alf}}$, that are on average much less than unity (*bottom panel*). Hence, even taking into account a latitudinal variation of $\tau_{\text{adv}} / \tau_{\text{Alf}}$, the magnetic field contributes very little to reviving the shock wave.

After this phase, a reduction of the mass accretion rate and a moderate contraction of the shock wave characterize the models, which settle into a state maintained for a time between several hundreds of milliseconds and about 3 s. Fairly constant neutrino luminosities translate into a timescale ratio $\tau_{\text{adv}} / \tau_{\text{heat}} \sim 0.3 \dots 0.6$. In models A08, A17, and A20, shock runaway is triggered by the quick decrease of the ram pressure corresponding to the infall of a shell interface located at a mass coordinate $m = 2.1 \dots 2.4 M_\odot$, while A05 reaches the transition to explosion without such an additional impulse due to a slow reduction of τ_{heat} over the course of about half a second. In the case of model A39, a non-negligible magnetic energy in the gain layer adds to the effect of neutrino heating and allows for an explosion at a much earlier time than in the other models ($t_{\text{exp}} \sim 0.4$ s).

The constraint of axisymmetry causes the ejecta to expand along the poles (Fig. 7). Variations in the fluxes of mass and energy lead to asymmetries of the outflows ranging from a moderate north-south imbalance to a unipolar geometry. Typically, the outflows coexist with cold inflows at lower latitudes that feed the growth of the PNS throughout the entire evolution after shock revival. The *bottom panel* of Fig. 7 displays the structure of the inflows/outflows in the central 600 km of the five neutrino-driven explosion models shortly before the end of the simulations. The inflows can take the form of narrow streams at high latitudes (A20), at lower latitudes (A39), as well as one-sided inflows across an entire hemisphere (A08). Transitions between these states also occur. Consequently, the PNS mass (Fig. 8, *top panel*) exceeds $M_{\text{PNS}} = 2 M_\odot$ before the end of the simulations in all cases. For models A20 and A39, the final values of $M_{\text{PNS}} \approx 2.55 M_\odot$ and $M_{\text{PNS}} \approx 2.42 M_\odot$ correspond to BH formation. While model A08 was terminated with a considerably lower PNS mass of $M_{\text{PNS}} \approx 2.2 M_\odot$, the rate of accretion is similar to that of the aforementioned models and, thus, the collapse to a BH is a plausible outcome, too. Note, however, that the long-term evolution of the PNS is not necessarily monotonic in terms of, e.g. its mass growth, especially if sufficiently strong poloidal magnetic fields develop (Paper II), as it is the case of model A08.

Models A05 and A17 show a transition to a phase in

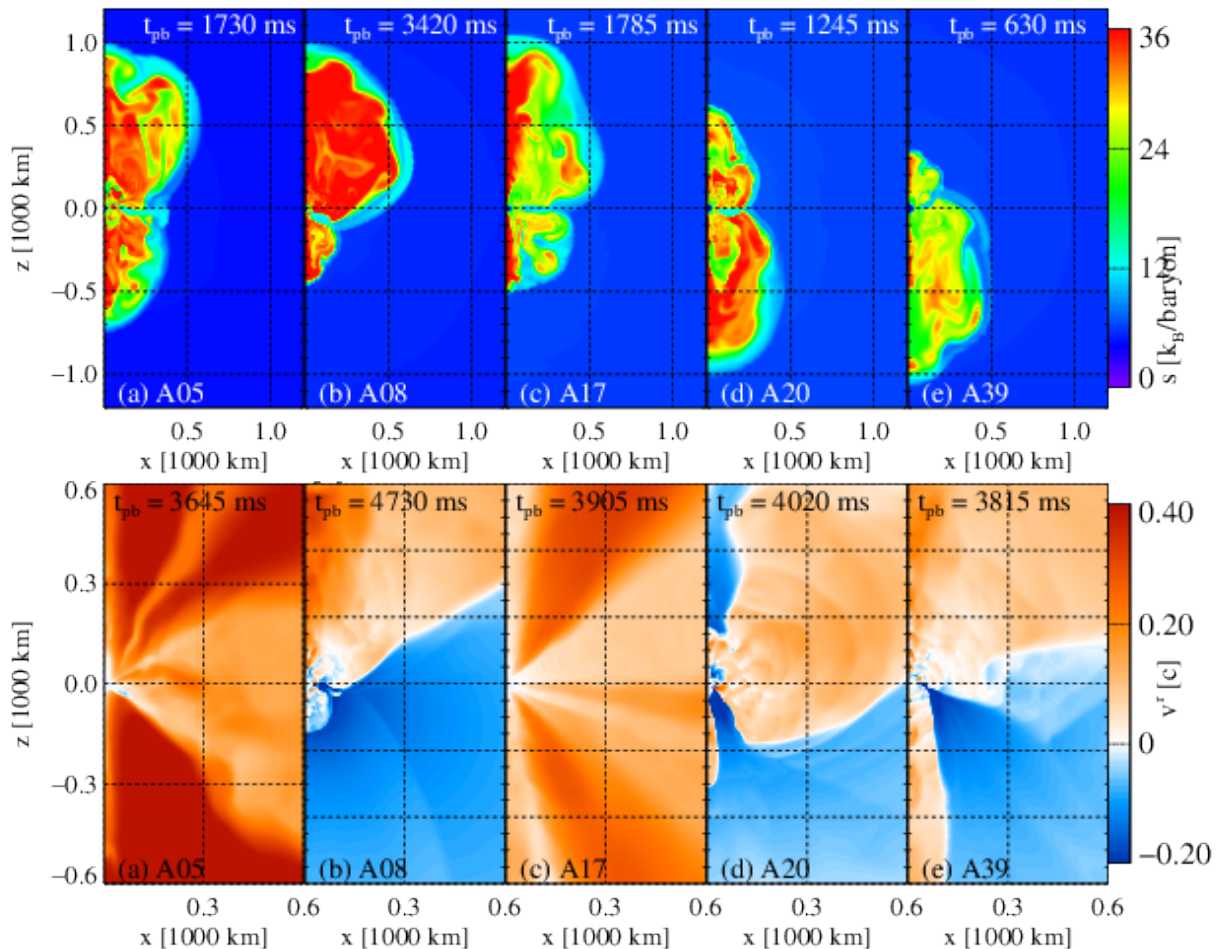


Figure 7. Top: Entropy maps of neutrino-driven explosions at the time when the shock wave has reached a maximum radius of $r_{\text{sh}} \approx 1000$ km. Bottom: maps of radial velocity towards the end of the runs.

which accretion ceases to occur after $t_{\text{pb}} > 3$ s. No inflows reach the PNS. While matter is ejected at all latitudes, the velocities and mass fluxes of the outflows are highest inside wide cones around the rotational axis (Fig. 7 *bottom panel*). At radii of a few 1000 km, these outflows are directed into wide polar jets (Fig. 7, *upper panel*). This configuration causes the PNSs to lose mass at rates of the order of $\dot{M}_{\text{PNS}} \sim -10^{-2} M_{\odot} \text{ s}^{-1}$ and signal a transient episode of PM spin-down (transient episodes of PM spin-down were also observed in models with sufficiently strong poloidal field in Paper II). We cannot precisely compute from our models the additional energy that the PM spin-down could add to the explosion. However, it is at least of the order of the free energy of the PNS differential rotation (e.g., Dessart et al. (2012); Paper II) or, at most, of the order of the PNS rotational energy (e.g. Metzger et al. 2011, 2015). Any process capable of redistributing angular momentum (e.g., the magnetorotational instability, viscosity, etc.) may potentially tap the shear energy and contribute to the SN explosion. For instance, viscosity may add extra heating to the postshock region (Thompson et al. 2005), while the magnetorotational instability may lead to a further growth of the magnetic field, driving a magnetorotational explosion (Paper I). As in Dessart et al. (2012) and Paper II we compute the free rotational energy by subtracting the rotational energy of

a rigidly rotating body with the same angular momentum, J_{PNS} and inertial momentum, I_{PNS} , from the total rotational energy of the PNS,

$$\mathcal{F}_{\text{PNS}} = \mathcal{T}_{\text{PNS}} - \frac{J_{\text{PNS}}^2}{2I_{\text{PNS}}} \quad (5)$$

(see Tab. 1). In the case of model A17, this value is greater than the explosion energy at the end of the simulation, $\mathcal{F}_{\text{PNS}} \approx 2.2 \times 10^{51}$ erg, while for A05 it accounts only for a minor correction to the explosion.

All PNSs possess a highrotational energy $\mathcal{T}_{\text{PNS}} > 10^{52}$ erg (see Tab. 1). Final values of the rotational energy correspond to ratios $-\mathcal{T}_{\text{PNS}}/E_{\text{PNS}}^{\text{grav}} \sim 0.5...2 \times 10^{-2}$ (Fig. 8, *second panel*), i.e., a range in which the PNS might be susceptible to non-axisymmetric instabilities. Besides amplification processes inside the PNS, the magnetization of the accreted matter drives the evolution of the magnetic energy. The final magnetic energies are typically two orders of magnitude lower than the rotational energies (Fig. 8, *bottom left panel*). Typical surface rotation rates reach a few 1000 s^{-1} (*upper right panel*) with models exploding mostly due to neutrino heating found at the lower end of the distribution of Ω_{srf} (hereafter, the subscript “srf” denotes average quantities over the PNS surface). The average magnetic fields on the PNS surfaces are dominated by a toroidal compo-

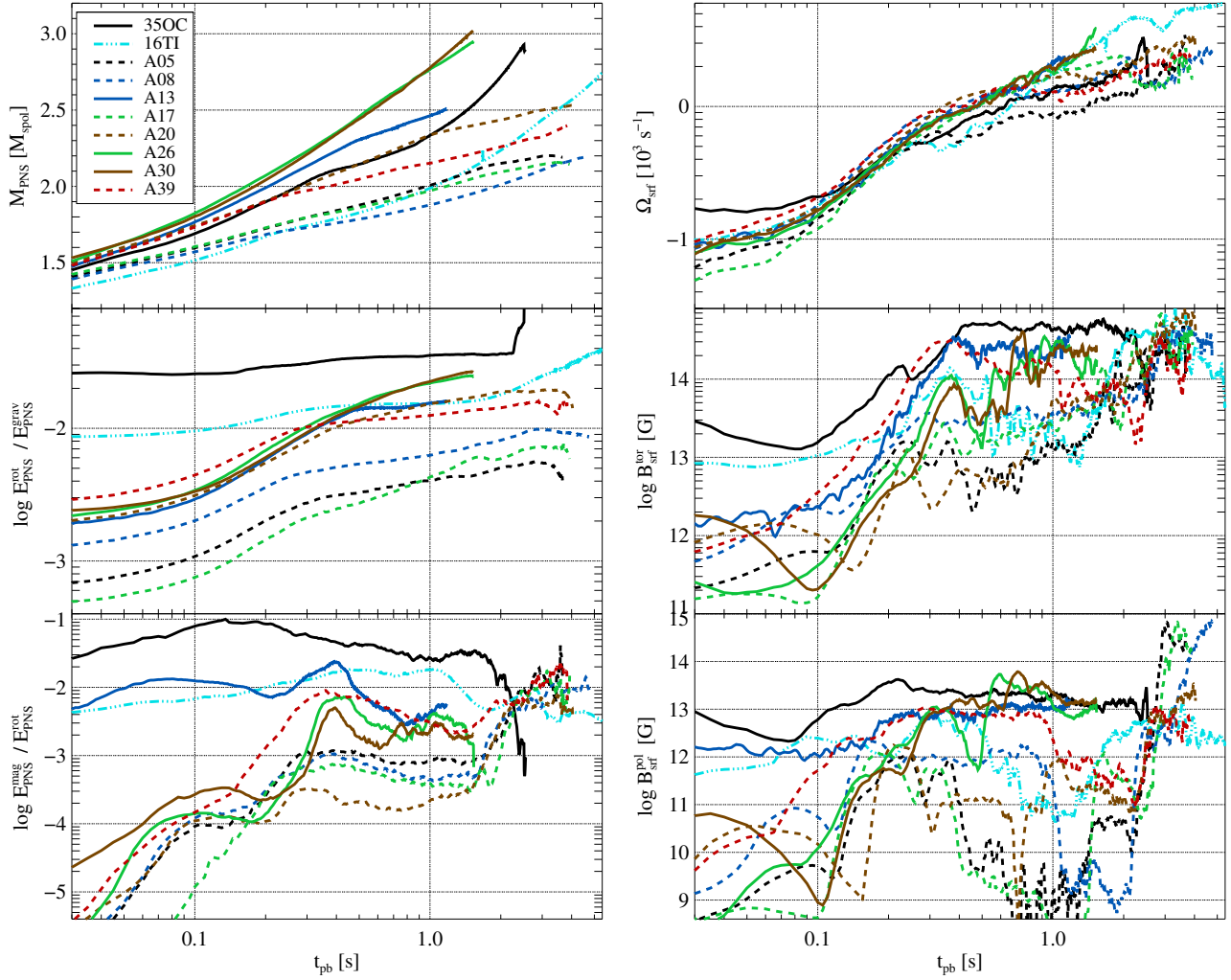


Figure 8. Left panel, top to bottom: evolution of the mass of the PNSs, the rotational energy normalized by the gravitational energy, and the magnetic energy normalized by the rotational energy. Right panel, top to bottom: averages of the rotational velocity, the toroidal and poloidal magnetic field strengths over the PNS surfaces.

ment of the order of $B_{\text{surf}}^{\text{tor}} \sim 10^{14...15}$ G (Fig. 8, *mid right panel*). The poloidal components (*bottom right panel*) tend to be considerably weaker during most phases of the evolution, in some cases down to a mere $B_{\text{surf}}^{\text{pol}} \sim 10^9$ G. As stated above, the suppression of the poloidal field proceeds in concert with the burial of the surface field by non-magnetized accreted layers. Likewise, the accretion of magnetized layers can lead to a quick rise of the poloidal field strength, exceeding $B_{\text{surf}}^{\text{pol}} \sim 10^{14}$ G and reaching equipartition with the toroidal component. Hence, the surface poloidal magnetic field of the models with smaller mass among the group that yields neutrino-driven explosions (A05, A08, and A17) grows to magnetar field strength after, at least $t_{pb} \sim 2.9$ s. Such conditions can favour the spin-down of the PNS and the transfer of its shear or rotational energy to the surrounding gas, which then is accelerated and forms the aforementioned wind-like outflows of models A05 and A17.

4.3 Magnetorotational explosions

Models whose explosions are launched mainly by magnetic fields and rotation (350C, A13, A30, and, to a slightly lower degree, A26) exhibit shock revival after at most $t_{\text{exp}} \lesssim 0.5$ s (Fig. 3) and a steady increase of the explosion energies and masses. For the two models based on progenitors with higher masses, A26 and A30, the energy increase proceeds faster than for the lower-mass model A13 as well as for model 350C. The progenitors of AD18 end with $E_{\text{exp}} \gtrsim 0.8 \times 10^{51}$ erg and $M_{\text{ej}} \gtrsim 0.3 M_{\odot}$.

The progenitors of this group possess more compact cores than those producing neutrino-driven explosions, with higher densities and compactness parameters outside a mass coordinate of $m \approx 1.8 M_{\odot}$ (Fig. 1). Models driving magnetorotational explosions also have larger values of M_4 and of μ_4 as their neutrino-driven counterparts. These differences, related to their Fe cores containing more mass, translate into higher mass accretion rates through the shock (*bottom panel* of Fig. 3) and lower neutrino luminosities w.r.t. the mass ac-

cretion rate, with ζ consistently remaining below those of neutrino-driven explosions (Fig. 4 *bottom panel*). These conditions make neutrino-driven shock revival more difficult to achieve.

The mass contained in the gain layers of these four models is on the upper end of the distribution (*top panel* of Fig. 6), while the rotational energies of the gain layer are lower than in the case of neutrino-driven explosions. The non-radial kinetic energies, on the other hand, do not systematically deviate from the other models, suggesting a similar level of hydrodynamic instabilities and turbulence. At least within the group of models from AD18, the same holds for the heating efficiency, η_{gain} (Fig. 6 *mid panel*). As a consequence, the models show a similar evolution of the advection-to-heating timescale ratio, $\tau_{\text{adv}}/\tau_{\text{heat}}$ with an early rise that by $t_{\text{pb}} \lesssim 200$ ms stops around $\tau_{\text{adv}}/\tau_{\text{heat}} \approx 0.8$, i.e., at values that can be regarded insufficient for launching an explosion (*bottom panel*).

Model 350C possesses a relatively high magnetic energy in the gain layer already shortly after bounce. The three models from AD18 start with a much weaker magnetization in the gain layer, but the accretion of extended layers with non-zero magnetic field (cf. Fig. 2) causes the magnetic energy to rise to values around $E_{\text{gain}}^{\text{mag}} \gtrsim 10^{47}$ erg. Models A13 and A30 explode shortly after that point. In these cases, the average ratio between the advection and the Alfvén timescale, $\tau_{\text{adv}}/\tau_{\text{Alf}}$, is still significantly lower than unity (Fig. 6, *bottom panel*). However, since the magnetic field is much stronger along the rotational axis than at lower latitudes, the Alfvén timescale becomes comparable to the advection timescale locally, giving rise to polar shock revival (as discussed in Paper I). The shock wave of A26 ceases to propagate after a short outward displacement and is revived only after a delay of another about 150 ms, when the timescales for neutrino heating and for Alfvén waves locally reach values similar to that of advection.

To a larger degree than for neutrino-driven shock revival, the different ejecta, whose entropy distributions are displayed in the *top panel* of Fig. 9 at the time when the maximum shock radius reaches 1000 km, are propagating in narrow jets along the rotational axis. The flow speeds in the jets reach up to $v^r \gtrsim c/3$ at radii of a few 1000 km with models A26 and A30 producing faster ejecta, followed by model A13. Inflows near the equatorial plane (see *bottom panel* of Fig. 9), found in all models, are persistent and lead to a comparably rapid growth of the PNS mass. Models A26 and A30 surpass the limit for stability of non-rotating neutron stars within less than ≈ 0.6 s. The growth proceeds until $M_{\text{PNS}}^{\text{A26, A30}} \approx 3 M_{\odot}$, at which point not even the rotational energy corresponding to $\mathcal{T}_{\text{PNS}}^{\text{A26, A30}} \approx 0.03 E_{\text{PNS}}^{\text{grav, A26, A30}}$ and a high degree of differential rotation can prevent the PNS from collapsing to a BH. Reaching gravitational instability takes longer for the less compact model A13. The magnetic influence on the explosion is not reflected in a particularly high magnetic energy of the PNSs. Compared to model 350C, the ratio of magnetic to rotational energy is lower by at least an order of magnitude. Indeed, the evolution of the ratio $E_{\text{PNS}}^{\text{mag}}/\mathcal{T}_{\text{PNS}}$ is very different in CHE models compared to the models of Woosley & Heger (2006). The former models possess much larger initial core rotational energies, which translate into ratios $E_{\text{PNS}}^{\text{mag}}/\mathcal{T}_{\text{PNS}}$ orders of magnitude smaller than in non-CHE models. The large differential energy reser-

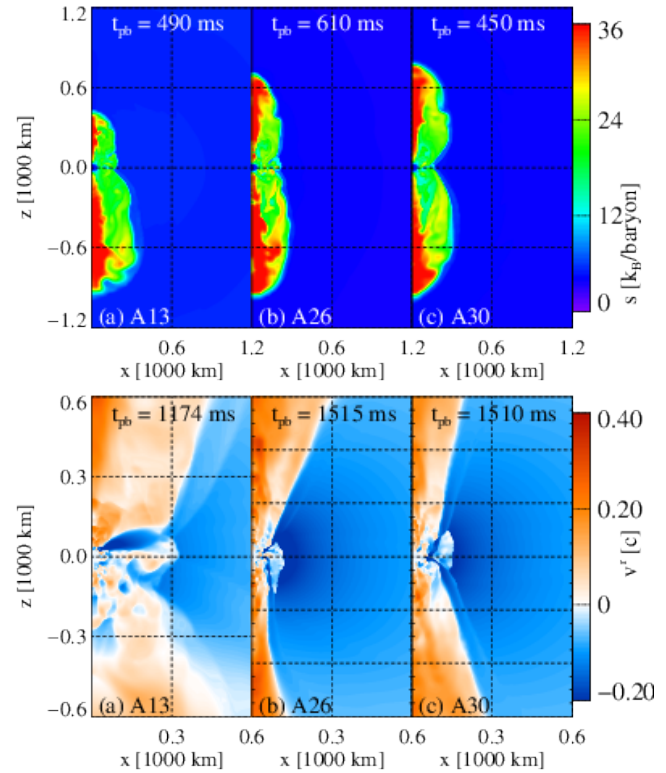


Figure 9. Same as Fig. 7, but for magnetorotational explosions.

voir of CHE models is partly tapped into by magnetic energy, making $E_{\text{PNS}}^{\text{mag}}/\mathcal{T}_{\text{PNS}}$ comparable to or larger than for non-CHE models after $t_{\text{pm}} \gtrsim 2$ s (Fig. 8 *bottom left*). The magnetic field strengths on the PNS surfaces, on the other hand, are much stronger than for the neutrino-driven explosions. The poloidal component in particular is consistently around $B_{\text{srf}}^{\text{pol}} \sim 10^{13}$ G.

Based on these results, we suggest that the presence of (moderately) strong, large-scale magnetic fields in the progenitor star connecting the PNS surface to and beyond the gain layer is the main reason for the ability of models 350C, A13, A26, A30 to launch explosions despite their high compactness and despite not featuring particularly high neutrino heating rates. It is precisely this subset of progenitors which possesses a magnetized layer around a mass coordinate of $m \approx 2 M_{\odot}$ (shaded regions in Fig. 2), whereas the absence of such a layers seems to preclude the possibility of MHD explosions. We note that the intermediate case of model A39 exhibits a magnetic field up to almost this mass coordinate and that the model A17 accretes a rather narrow shell with non-vanishing magnetic field around the time when it accelerates a late outflow resembling PM winds. Thus, we find a connection between the PM activity and the topology of the magnetic field in the stellar progenitor. Unfortunately, current stellar evolution models cannot accurately obtain the topology of the field in the pre-collapse stage (e.g. Paper II). Model A05 produces a similar outflow after the (poloidal) PNS surface field has grown by several orders of magnitude without accreting a magnetized layer. This suggests a second way to create the field configuration necessary to launch such an outflow by transporting field from the interior of the PNS to its surface or amplifying it locally.

4.4 Failed explosion

The evolution of model 16TI is affected strongly by its very rapid rotation. In the innermost $m \approx 2 M_\odot$, its initial density profile, the compactness derived from it, and the parameters M_4 and μ_4 roughly fall into the range established by models exploding due to neutrino heating. Consequently, the mass accretion rate is, at least at early times, comparable to those. At the same time, centrifugal support reduces the release of gravitational energy from the matter falling onto the PNS, thus lowering the neutrino luminosity. After $t_{\text{pb}} \approx 0.25$ s, when the entire inner core has been accreted, this reduction becomes less important, but then a relatively shallow density profile causes the mass accretion rate to drop only slowly. Measured in terms of the mass accretion rate, the neutrino luminosity never gets high enough to trigger an explosion with $\zeta \sim 0.4$ for most of the evolution. Until $t_{\text{pb}} \sim 2$ s, neutrino heating is still fairly important in a gain layer whose mass is shrinking below $M_{\text{gain}} < 10^{-3} M_\odot$. Advection through the gain layer remains faster than neutrino heating, though only by a factor of about 2.

We note that model A39 launches an explosion under conditions that are not too dissimilar from the state of failing model 16TI. The former model, however, possesses a magnetic field that is sufficiently strong to aid in the process of reviving the shock wave. In model 16TI, on the other hand, once the entire Fe core has fallen onto the PNS, the ensuing drop of the mass accretion rate goes along with a transition to the accretion of a non-magnetized shell. We note the essentially unmagnetized structure of model 16TI for $1.8 \lesssim m/M_\odot \lesssim 8.8$ compared to the unmagnetized shell surrounding the core of model A39 for $2 \lesssim m/M_\odot \lesssim 4.6$ in Fig. 2. Hence, the magnetization of the gain layer drops, eliminating the prospects of an explosion due to a mixed neutrino-MHD mechanism like in model A39. Again, the topology of the magnetic field in the progenitor star is determinant for the fate of the post-collapse system.

Failing to launch an explosion, M_{PNS} steadily increases until it will unavoidably produce a BH. By $t_{\text{pb}} \gtrsim 3$ s, the PNS exceeds the limit for stability for a non-rotating NS. However, its very high rotational energy delays the collapse by several seconds and allows for the accretion of additional mass. Indeed, model 16TI has not formed a BH even after $t_{\text{pb}} = 6.1$ s.

In the time interval $t_{\text{pb}} \approx 2.6 \dots 3.2$ s, the layers located in the progenitor at Lagrangian mass coordinates $m \approx 2.32 \dots 2.45 M_\odot$ are falling onto the PNS. These layers possess a particularly high specific angular momentum in excess of our estimates for the angular momentum corresponding to the last stable orbit for a maximally rotating Kerr BH encompassing all the matter enclosed by them (Fig. 2; note the yellow dashed line). To illustrate the effect of rotation on the structure of the core, we compare the profiles of $j(m)$ in the equatorial plane for several times (solid lines in the *top* panel of the figure) to the specific angular momentum of matter in Keplerian rotation about the centre, defined as $j_{\text{Kep}} = r^2 \sqrt{-\Phi}$, where Φ is the gravitational potential (dashed lines). Where $j > j_{\text{Kep}}$, centrifugal forces can stop accretion onto the PNS, which is the case during this phase. Consequently, we observe the formation of a small rotationally supported torus just above the PNS surface. As displayed in Fig. 11 for $t_{\text{pb}} = 2.8$ and 3.1 s, this

torus is adjacent to the PNS and extends from its surface to about twice its radius. The torus is composed of matter with densities of $\rho > 10^{11} \text{ g cm}^{-3}$ (black contours). This high density makes it partially optically thick to neutrinos and the neutrinospheres (pink lines) encompass large swaths of it. In the central regions of the torus, the emission of neutrinos occurs on rapid timescales compared to the dynamics and dominates over their absorption. Consequently, the matter approaches an equilibrium state characterized by low entropy and low electron fraction, the absorption equilibrium of Just et al. (2021).

Since the distribution of j shows an abrupt decline toward higher radii, gas accreted after $t_{\text{pb}} \approx 3.2$ s comes with much lower specific angular momentum. After only a brief time, the centrifugal support of the torus no longer suffices to balance gravity and the ram pressure of the newly accreted gas, and the torus breaks down and is quickly absorbed by the PNS. In the subsequent seconds of the evolution, the specific angular momentum of the accreted gas remains below the Keplerian value by a factor of a few. The structure of the core does not change from the state displayed in the *right* panel of Fig. 11. Only a very thin layer of hot gas with high electron fraction separates the PNS from the infalling matter. This configuration may only change when the PNS collapses to a BH or when the next layer with potentially super-Keplerian rotation, located at a mass coordinate of $m \approx 3.1 M_\odot$ will be accreted. Until this point, the PNS can only sustain itself against its own gravity due to its fast rotation. Hence, any sufficiently efficient process leading to a loss of angular momentum to the exterior or a flattening of the differential rotation (e.g., non-axisymmetric instabilities) might lead to BH collapse before the accretion of this layer can produce another PNS-plus-torus system.

We note that we had observed the formation of a qualitatively similar system in previous models such as 350C-Rw, 350C-RRw or 350B-RRw (Paper II), which also show a very extended disc around the PNS. In that case, however, the disc formation was an inside-out process driven by the magnetic transport of angular momentum from the centre of the PNS to its outer layer, which consequently gains centrifugal support and expands. Here, on the other hand, the torus is formed due to the high angular momentum the gas possesses already in the pre-collapse star. Hence, contrary to the inside-out mechanism, for which the disc forms from gas belonging to the PNS, the outside-in process relies on neutrino emission to drive Y_e to the low values we find in model 16TI.

5 POTENTIAL FUTURE EVOLUTION

Since the dynamics that our models undergo happens deep inside of a massive star, electromagnetic radiation cannot escape out of the region of interest and yield an observable signal. Only gravitational waves, neutrinos, and the nucleosynthetic yields formed at this early stage of the explosion may inform us about the dynamics of our simulations. However, large uncertainties beset any attempt to determine the type of explosion from the state of our models at this point. In addition to the diagnostic explosion energies, ejecta geometries and the type of compact remnant, we aim here at providing very rough estimates of (i) the mass of radioactive

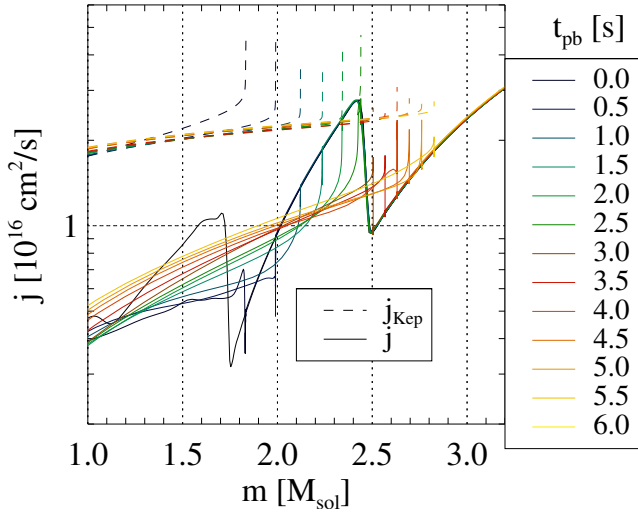


Figure 10. Profiles of the actual specific angular momentum in the equatorial plane of model 16TI (solid lines) compared to the Keplerian specific angular momentum (dashed lines).

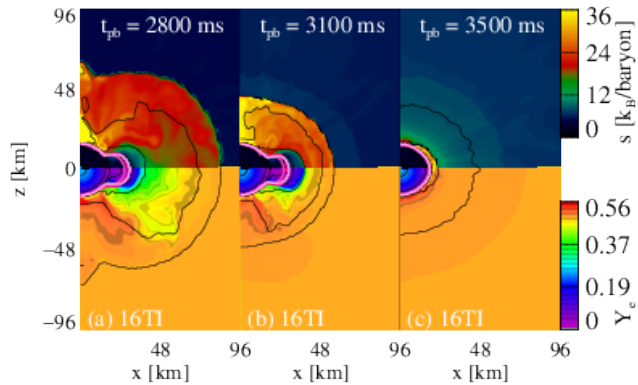


Figure 11. Specific entropy and electron fraction (colour maps) together with isodensity lines ($\rho = 10^{15,14,13,\dots} \text{g cm}^{-3}$, black lines) and the neutrinospheres (pink lines) of model 16TI around the temporary formation of a rotationally supported disc around the PNS.

Ni synthesized and ejected, and (ii) of the early bolometric light curves.

5.1 Estimation of the Ni mass

A relatively large amount of Ni mass synthesized during the early phases of the explosion could explain the high luminosity of SLSNe or HNe. As we shall show in this section, this is not the case in our models.

In a manner similar to the flashing scheme that our EOS uses to determine the composition of the baryonic component of the gas (Rampp & Janka (2002); Müller et al. (2016)), we assume that a fraction $f_{\text{Ni}} \leq 1$ of all lighter elements contained in an unbound fluid element of the ejecta is immediately burned to Ni once the temperature exceeds a threshold of $T_{\text{Ni}} = 5 \text{ GK}$. At sufficiently high entropy per baryon, photodisintegration of Ni into α particles may significantly limit the amount of Ni synthesized. Following Surman et al. (2011), Hayakawa & Maeda (2018), we account for this effect

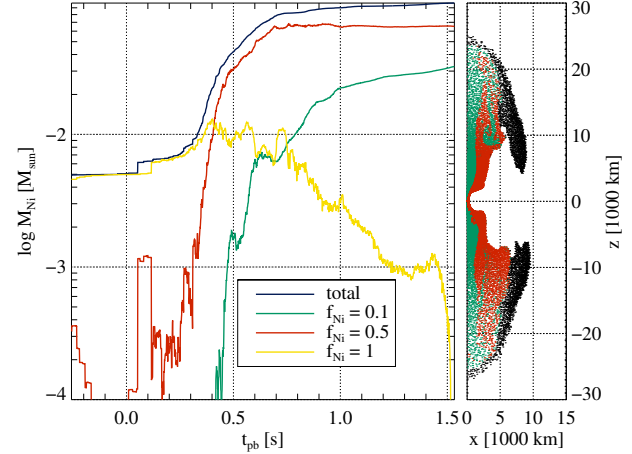


Figure 12. *Left panel:* time evolution of the ejected Ni mass of model A30. The dark blue line represents the total Ni mass, and the coloured lines show the mass contained in gas with a production factor f_{Ni} as indicated in the legend. *Right panel:* spatial distribution of unbound fluid elements at the end of the simulation. Black symbols stand for Lagrangian tracers that do not contain any Ni, while tracers with $f_{\text{Ni}} = 0.1, 0.5, 1$ are displayed by the same colours as in the *left panel*. The yellow Lagrangian tracers are very scarce at the end of the computed time and, hence, hardly visible at the interface between the jet cavity and the progenitor star.

by computing the specific entropy of the baryons,

$$s_b = \frac{4a_{\text{rad}}m_p T^3}{3\rho k_B}, \quad (6)$$

where a_{rad} , m_p , and k_B are the radiation constant, the proton mass, and Boltzmann's constant, respectively. The Ni fraction depends on s_b ,

$$f_{\text{Ni}} = \begin{cases} 1 & \text{for } s_b < 1, \\ 0.5 & \text{for } 1 < s_b < 10, \\ 0.1 & \text{for } 10 < s_b. \end{cases} \quad (7)$$

In practice, we record the evolution of Lagrangian tracer particles. If the temperature of a tracer surpasses T_{Ni} , we assign it a fraction of Ni according to its entropy. This fraction can change as long as the temperature is higher than T_{Ni} . After cooling below this value, we assume that the composition freezes out.

Note that our simulations use an EOS that contains, in addition to baryons, also leptons and photons. These additional components make the entropy in our simulations in general greater than the approximation of Hayakawa & Maeda (2018). To use their recipe together with our EOS, we would have to recalibrate the entropy thresholds to account for the systematic differences. Such an improvement of the method would require a detailed comparison to the conditions for NSE and is beyond the scope of this article. We cautionary note that our simple estimates can be off by several 10%.¹ Thus, we only use them to obtain general

¹ For comparison, using a detailed nucleosynthesis network, Reichert et al. (2021) obtained $M_{\text{Ni}} = 0.0473 M_{\odot}$ for model 350C. For the same model, we obtain $M_{\text{Ni}} = 0.048 M_{\odot}$ with the simplified method described here. The striking similarity of the results should not be taken as a measure of the goodness of the simpli-

tendencies within our set of stars. The last column of Tab. 1 (M_{Ni}) lists the results.

We discuss first a representative case, namely model **A30**, for which Fig. 12 shows both the time evolution of the Ni mass (left panel) and the spatial distribution of Ni at the final time (right panel). Some of the fluid elements that will be ejected already contain Ni before bounce, $t_{\text{pb}} < 0$. At that time, they possess low entropy and, thus, consist entirely of Ni ($f_{\text{Ni}} = 1$, yellow line in the *left panel*). In the first phase after bounce, most ejecta that surpass T_{Ni} do so at low entropy and therefore belong to the same group. However, as neutrino heating and shock waves in the jet increase the entropy of the tracers, some of the Ni is dissociated and f_{Ni} decreases for the aforementioned fluid elements. Additional Ni production occurs mostly in tracers with higher entropy and, thus, low values of $f_{\text{Ni}} = 0.5$ and 0.1 (red and green lines, respectively). At the end of the simulation, gas with $f_{\text{Ni}} = 0.5$ dominates the Ni content of the model, mostly distributed in the cocoon of the jet (red points in the *right panel*), while the jet beam contains matter with higher entropy and $f_{\text{Ni}} = 0.1$ (green symbols). Surrounding the jets we find ejecta that never reached the threshold temperature for Ni formation.

At first glance, our models synthesize insufficient Ni mass to even explain typical CCSNe, which yield $\sim 0.1M_{\odot}$ of Ni. Even less can they account for more energetic hypernovae, which produce larger amounts of Ni (Iwamoto et al. 1998; Drout et al. 2011; Lyman et al. 2016). However, we first note that all our models, save for the non-exploding model **16TI**, show (diagnostic) explosion energies of the order of the canonical value of $E_{\text{exp}} = 10^{51}$ erg or more (see Tab. 1). Extrapolating to subsequent phases, further growth is possible, unless the collapse of the PNS to a BH shuts down the injection of energy into the surrounding gas. Should a BH form, further Ni can be synthesized in the winds emerging from the accretion disk (e.g. MacFadyen et al. 2001; Kohri et al. 2005; Kumar et al. 2008; Hayakawa & Maeda 2018), that will surround the BH after the formation of a collapsar. Exploring further this regime is beyond the scope of this paper. Also, explosive nucleosynthesis due to the interaction of the accretion disc wind with the stellar envelope may yield some extra Ni production (Woosley & Weaver 1995; Maeda & Tominaga 2009). However, this mechanism tends to operate once the BH is sufficiently massive, as it has swallowed most of the stellar envelope. That limits the availability of envelope materials for explosive nucleosynthesis (Maeda & Tominaga 2009), specially in CHE models with masses below, say, $8M_{\odot}$ (i.e., **A05**, and **A08**). These models may, at most, form BHs as massive as their initial pre-SN mass minus the ejecta mass. Neutrino-driven explosions are systematically less violent than magnetorotational ones. After a shock revival powered by neutrino heating, models **A05** and **A17** enter a PM-like phase in which the explosion energy increases at very high rates. While all explosions show an asymmetric geometry, to a certain degree enforced by the assumption of axisymmetry, a stronger contribution of magnetic fields to the explosion enhances this tendency.

fied treatment. Applied to other models of Reichert et al. (2021), discrepancies of a few 10% are found.

5.2 Approximate bolometric light curves

In order to gain further insight on the kind of high-energy transient that our models yield, we have computed approximate analytic light curves due to the radioactive decay of Ni based upon Dado & Dar (2015). For more elaborate models including 3D Monte-Carlo simulations we refer the reader to, e.g. Vurm & Metzger (2021). Our models, furthermore, develop compact cores with large rotational energy ($\mathcal{T}_{\text{PNS}} > 10^{52}$ erg). Hence, we also include the contribution of a central energy source that may tap a fraction of the core's rotational energy, thermalize it with the SN ejecta, and may modify the early bolometric light curve. We consider separately cases which do not produce a BH during the computed time (**A05**, **A08**, and **A17**) from the rest of the progenitors that undergo CHE. Models that do not produce BHs, possess adequate conditions for hosting a PM, and we refer collectively to them as proto-magnetar candidates (PMCs). Indeed, one of them has already shown transient PM spin-down activity (model **A17**). Thus, their light curves may display signatures of a central PM engine on longer terms than calculated in this work. For the rest of the models, we assume that the spin-down of the BH constitutes the central engine of a GRB (Nathanail & Contopoulos 2015; Nathanail et al. 2016), in which part of the BH released energy will be transferred to the SN ejecta.

The radioactive contribution to the light curve follows exactly the analytic estimation of Dado & Dar (2015), taking as inputs from our models the Ni Mass (Tab. 1), the ejecta asymptotic velocity, V_{ej} , and the ejecta mass, \mathcal{M}_{ej} . All these quantities are approximate and not the result of a sufficiently long and detailed calculation. We estimate an upper bound to the ejecta mass as the difference between the stellar mass at the brink of collapse, M_0 , and the PNS mass at $t_{\text{pb}} = t_{\text{f}}$ (i.e. $\mathcal{M}_{\text{ej}} := M_0 - M_{\text{PNS}}(t_{\text{f}})$). We note that \mathcal{M}_{ej} is significantly larger than the mass unbound at $t_{\text{pb}} = t_{\text{f}}$ (M_{ej} ; see Fig. 3) or the mass enclosed by the shock at that time ($M_{\text{sh,e}}$; Tab. 1). At $t_{\text{pb}} = t_{\text{f}}$ the explosion is ongoing and both M_{ej} and $M_{\text{sh,e}}$ are still growing until they reach their final values. The asymptotic ejecta velocity is estimated as $V_{\text{ej}} = \sqrt{2E_{\text{k}}/\mathcal{M}_{\text{ej}}} = \sqrt{2(\mathcal{T}_{\text{PNS}}f_{\text{er}} + E_{\text{exp}})/\mathcal{M}_{\text{ej}}} \approx \sqrt{2\mathcal{T}_{\text{PNS}}f_{\text{er}}/\mathcal{M}_{\text{ej}}}$, where we allow for the possibility that only a fraction f_{er} of the PNS rotational energy can be converted into kinetic energy of the ejecta, E_{k} . The last approximation results from the fact that the \mathcal{T}_{PNS} ($> 10^{52}$ erg) is one order of magnitude (or more) larger than E_{exp} ($< 2 \times 10^{51}$ erg; see Tab. 1). Typical ejecta velocities in all our models are $V_{\text{ej}} \approx (0.4 - 1.6) \times 10^9$ cm s $^{-1}$. The corresponding luminosity reads (Dado & Dar 2015)

$$L_{\text{nuc}}(t) = \frac{e^{-t^2/2t_{\text{r}}^2}}{t_{\text{r}}^2} \int_0^t x e^{x^2/2t_{\text{r}}^2} \dot{E} dx, \quad (8)$$

where

$$t_{\text{r}} = \sqrt{\frac{3\mathcal{M}_{\text{ej}}f_{\text{e}}\sigma_{\text{T}}}{8\pi m_{\text{p}}cV_{\text{ej}}}}, \quad (9)$$

σ_{T} is the Thompson cross section, m_{p} the proton mass, c the light speed, $f_{\text{e}} \approx 0.275$ is the fraction of free electrons,

Model	$L_{\text{pm},47}$ [erg s $^{-1}$]	$B_{\text{srf},14}^{\text{pol}}$ [G]	$\bar{\Omega}$ [Hz]	R_{PNS} km	$I_{\text{PNS},45}$ [g cm 2]	t_{pm} [days]	$L_{\text{pk},43}$ [erg s $^{-1}$]	t_{pk} [days]	t_{r} [days]	\mathcal{M}_{ej} M_{\odot}	$V_{\text{ej},9}$ [cm s $^{-1}$]	$E_{\text{k},52}$ [erg]
A05	2.96	3.37	2794	17.3	2.61	0.208	15.1	9.02	14.2	2.81	1.6	0.72
A08	35.1	7.73	3143	18.0	3.26	0.030	2.64	10.9	22.9	5.80	1.3	0.95
A17	28.8	4.00	3368	20.4	2.45	0.035	0.82	20.9	46.0	14.9	0.82	0.98

Table 2. Properties of models with potential PM activity: model name, engine luminosity, surface average poloidal magnetic field of the PNS, representative rotational frequency, PNS equivalent spherical radius, PNS moment of inertia, decay time of the spin-down luminosity, total luminosity maximum time, total luminosity maximum, effective photon diffusion time, ejecta mass, ejecta velocity, and ejecta kinetic energy. We use the convention $A_x = A/10^x$ to express various quantities in the table. A value $f_{\text{er}} = 0.5$ is used for the calculation of L_{pm} and other derived magnitudes. All the properties of our models are obtained at $t = t_{\text{f}}$.

Model	$L_{\text{pm},47}$ [erg s $^{-1}$]	$B_{\text{srf},14}^{\text{pol}}$ [G]	$\bar{\Omega}$ [Hz]	R_{PNS} km	$I_{\text{PNS},45}$ [g cm 2]	t_{BZ} [days]	$L_{\text{pk},43}$ [erg s $^{-1}$]	t_{pk} [days]	t_{r} [days]	\mathcal{M}_{ej} M_{\odot}	$V_{\text{ej},9}$ [cm s $^{-1}$]	$E_{\text{k},52}$ [erg]
A13	0.150	0.259	2864	26.7	7.02	3.53	9.79	17.8	41.3	10.5	0.72	0.53
A20	0.147	0.236	5134	18.3	3.53	4.22	6.83	22.7	59.1	17.5	0.58	0.58
A26	1.47	0.553	4785	25.5	6.87	0.657	1.51	6.09	64.8	23.1	0.64	0.93
A30	1.43	0.520	4589	34.1	8.00	0.728	1.49	6.75	71.0	27.0	0.62	1.04
A39	0.02	0.095	3981	24.1	4.27	27.7	7.31	87.6	109	36.6	0.36	0.47

Table 3. Same as Tab. 2 but for models with potential BH spin-down activity. Instead of listing the decay time of the spin-down luminosity, we provide the decay time of the Blandford-Znajek process.

and $\dot{E} = \dot{E}_{\gamma} + \dot{E}_{e+}$, where

$$\dot{E}_{\gamma} = \frac{M_{\text{Ni}}}{M_{\odot}} \left[7.78 A_{\gamma}^{\text{Ni}} e^{-t/8.76 \text{ d}} + 1.50 A_{\gamma}^{\text{Co}} \left[e^{-t/111.27 \text{ d}} - e^{-t/8.76 \text{ d}} \right] \right] 10^{43} \text{ ergs}^{-1} \quad (10)$$

is the power supplied by γ -rays, and

$$\dot{E}_{e+} = \frac{M_{\text{Ni}}}{M_{\odot}} A_e \left[e^{-t/111.27 \text{ d}} - e^{-t/8.76 \text{ d}} \right] 10^{43} \text{ ergs}^{-1}, \quad (11)$$

is the power supply in the form of the kinetic energy of positrons. $A_e \approx 0.05$ is the ratio of the energy released as positron kinetic energy and as γ -ray energy in the decay of ^{56}Co . A_{γ}^{Ni} and A_{γ}^{Co} are the absorbed fractions of the γ -ray energy in the SN ejecta from the decay of ^{56}Ni and ^{56}Co , respectively. They are computed as $A_{\gamma} \approx 1 - e^{-\tau_{\gamma}}$, with $\tau_{\gamma} = 3M_{\text{ej}}\sigma_t/(8\pi m_p V_{\text{ej}}^2 t^2)$, and $\sigma_t = 9.5 \times 10^{-26} \text{ cm}^2$ ($\sigma_t = 8.7 \times 10^{-26} \text{ cm}^2$) for ^{56}Ni (^{56}Co).

In order to incorporate the contribution of the PM to the light curves we follow the same lines as KB10. We assume that the magnetar injects a luminosity due to the spin-down of the PNS in the ejecta given by

$$L_{\text{pm}}(t) = \frac{\mathcal{T}_{\text{PNS}} f_{\text{er}}}{t_{\text{pm}}} \frac{1}{(1 + t/t_{\text{pm}})^2}, \quad (12)$$

where the typical decay time of the spin-down luminosity is

$$t_{\text{pm}} = \frac{6I_{\text{PNS}}c^3}{(B_{\text{srf}}^{\text{pol}})^2 R_{\text{PNS}}^6 \bar{\Omega}^2}. \quad (13)$$

To compute t_{pm} we use various inputs taken from the PNS in each model at $t = t_{\text{f}}$ (see Tab. 2), namely the moment of inertia (I_{PNS}), the equivalent spherical radius ($R_{\text{PNS}} = (3V_{\text{PNS}}/4\pi)^{1/3}$; V_{PNS} is the PNS volume), the surface averaged poloidal magnetic field, and a representative rotational frequency ($\bar{\Omega} = \sqrt{2\mathcal{T}_{\text{PNS}}/I_{\text{PNS}}}$). As a result, we obtain values of t_{pm} significantly smaller than the effective photon diffusion

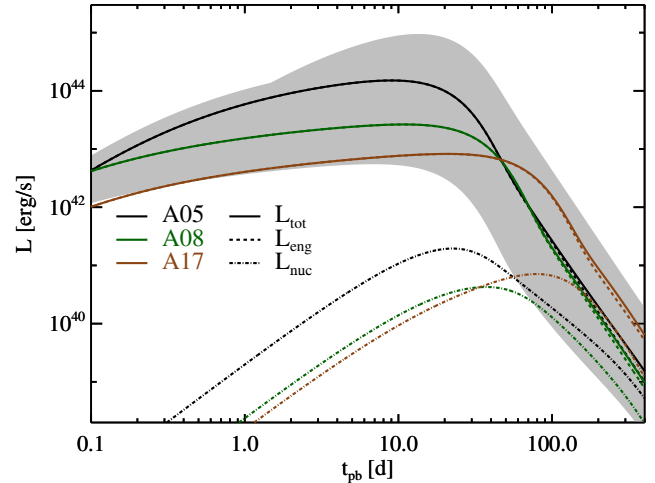


Figure 13. Solid lines: Approximate bolometric light curves of models that yield successful SNe and have not produced a BH in the course of the computed time. Dashed lines: extrapolated light curves produced by a PM with the same surface poloidal magnetic field and rotational period than the PNS of the models indicated in the legends. For both the solid and dashed lines, we assume that the ejecta energy is only a fraction $f_{\text{er}} = 0.5$ of the available PNS rotational energy and may eventually produce photons that contribute to the light curve. Dash-dotted lines: analytic light curves produced by the radio active decay of the same mass of Ni as in our models. Grey region: approximate range of uncertainty of the predicted bolometric light curve of model A05. The upper (lower) boundary assumes $f_{\text{er}} = 0.9$ and $f_{\text{pm}} = 10$ ($f_{\text{SN}} = 0.01$ and $f_{\text{pm}} = 0.1$).

time (compare t_{pm} and t_{r} in Tab. 2). These small values of t_{pm} contrast with the ones of ~ 1 yr employed in KB10 or those of Nicholl et al. (2017) (who estimated $t_{\text{pm}} \sim 5$ days for the Gaia16apd SLSN). The smaller values of t_{pm} in our

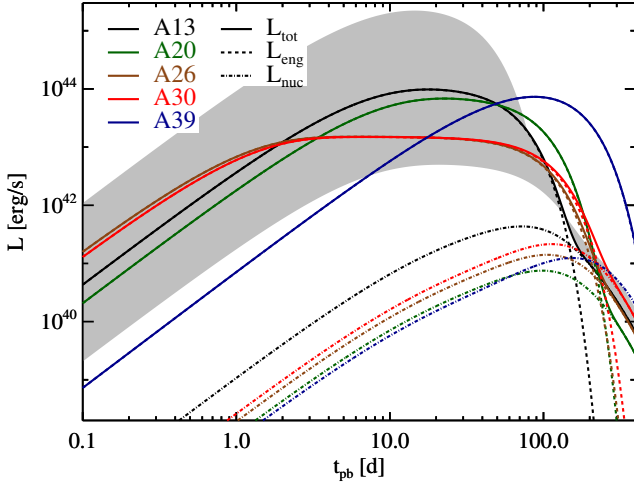


Figure 14. Solid lines: Approximate bolometric light curves of models that undergo a CHE, yield successful SNe and have produced a BH in the course of the computed time. Dashed lines: extrapolated light curves produced by the Blandford-Znajek spin-down of a BH with the same surface poloidal magnetic field at the outer horizon and mass as that of the PNS right before BH collapse. For both the solid and dashed lines, we assume that the ejecta energy is only a fraction $f_{\text{SN}} = 0.1$ of the available BH rotational energy and may eventually produce photons that contribute to the light curve. Dash-dotted lines: analytic light curves produced by the radio active decay of the same mass of Ni as in our models. Grey region: approximate range of uncertainty of the predicted bolometric light curve of model A13. The upper (lower) boundary assumes $f_{\text{SN}} = 0.9$ ($f_{\text{SN}} = 0.01$).

case stem from the typically larger surface average magnetic fields, PNS radii and PNS inertia moments, and the fact that the typical periods of the PNSs at hand are ~ 2 ms.

Finally, we compute the contribution to the light curve of the PM central engine as

$$L_{\text{eng}}(t) = \frac{e^{-t^2/2t_r^2}}{t_r^2} \int_0^t x e^{x^2/2t_r^2} L_{\text{pm}}(x) dx. \quad (14)$$

In expression (14) we are implicitly assuming that the engine’s luminosity is efficiently reprocessed into thermal radiation, and that this is injected at the inner edge of the ejecta. This is a common assumption in the literature (KB10; Dessart et al. (2012); Inserra et al. (2013); Metzger et al. (2015); Nicholl et al. (2017)). The total bolometric light curve is then

$$L_{\text{tot}}(t) = L_{\text{eng}}(t) + L_{\text{nuc}}(t). \quad (15)$$

We display in Fig. 13 the bolometric light curves of PMCs along with the separate contributions of $L_{\text{eng}}(t)$ and $L_{\text{nuc}}(t)$. The contribution of the central PM engine dominates the light curve until well beyond the luminosity peak, L_{pk} . The smaller the progenitor mass, the sooner the luminosity reaches its maximum value and the larger is L_{pk} . To understand this behaviour, we first notice that there is a direct correlation between the progenitor mass and the ejecta mass. Since all models develop compact cores with masses clustering in the range $M_r \simeq 2.2M_{\odot} - 3M_{\odot}$, and $M_{\text{ej}} := M_0 - M_{\text{PNS}}(t_f)$, the ejecta mass is roughly proportional to the stellar progenitor mass in our simple light curve model. The larger peak luminosity for less massive progenitors comes from the fact that $L_{\text{pk}} \sim \mathcal{T}_{\text{PNS}} t_{\text{pm}} f_{\text{er}} / t_r^2 \propto \mathcal{M}_{\text{ej}}^{-3/2}$

(KB10). The earlier peak time associated to the smaller progenitor mass stems from the dependence of the effective diffusion time with the ejecta mass, $t_r \propto \mathcal{M}_{\text{ej}}^{1/2}$ (Eq. 9). At this point it is convenient to reiterate that the ejecta mass that we are using is significantly larger than M_{ej} and $M_{\text{sh,e}}$ (especially for model A17, though $M_{\text{sh,e}} \approx M_{\text{ej}}$ for A05). Should the true ejecta mass be smaller than our upper bound, our models would produce even brighter light curve peaks at earlier times. The highest possible luminosities in an engine driven light curve happen when $t_{\text{pm}} \sim t_r$ (KB10). This is not the case in our PMCs, where typically $t_r \gg t_{\text{pm}}$. Hence, we expect that the peak time be $t_{\text{pk}} \sim t_{\text{pm}} / (\ln(t_r/t_{\text{pm}}) - 1)^{1/2} \sim 0.4t_{\text{pm}}$ (KB10). The relation approximately applies to PMCs, as can be checked from Tab. 2.

Given the strong dependence of the light curve on the spin-down timescale and on the fraction of the engine’s energy that may be transferred to the ejecta, we roughly quantify the uncertainty in our approximate light curves as follows. First, we allow for the possibility that t_{pm} be a factor f_{pm} longer or shorter than the estimation of (12). This is justified because the conditions of the PNS at $t_{\text{pb}} = t_f$ may experience some evolution on longer time scales (Paper II), and also be affected by the fallback of matter not unbound during the explosion. Second, we anticipate that not all the rotational energy may be transferred to the ejecta. Also, as the rotational energy of the PNS decreases below $\sim 10^{50}$ erg s $^{-1}$ the energy loss may decrease (Bucciantini et al. 2009). The PM injected energy can produce a collimated relativistic jet if the magnetic to total energy ratio is large enough (Bucciantini et al. 2007). In this case, the jet may penetrate the SN ejecta without releasing most of its energy in them, instead producing a GRB (Bucciantini et al. 2008). The upper boundary of the grey-shaded area in Fig. 13 corresponds to model A05 using an spin-down time scale $f_{\text{pm}} = 10$ longer than the estimation of (12) ($t_{\text{pm}} \approx 0.2$ days) and assuming that most of the PNS rotational energy is efficiently transferred to the SN ejecta ($f_{\text{er}} = 0.9$). The lower boundary of the uncertainty band results from taking a 10 times shorter spin-down time scale ($f_{\text{pm}} = 0.1$) and a relatively low efficiency for the energy transfer ($f_{\text{er}} = 0.1$). Even under these assumptions, the light curve of model A05 has a relatively large (engine-driven) peak luminosity $\sim \text{few} \times 10^{42}$ erg s $^{-1}$.

There is a factor ~ 3 between the largest and the smallest Ni mass of PMCs (Tab. 1). Due to the proportionality between L_{nuc} and M_{Ni} , this radioactive mass difference reflects in the peaks of L_{nuc} in our models. Besides this factor, the contribution of the radioactive Ni decay is only observable well beyond t_{pk} if the spin-down timescale is significantly shorter than the estimation of (13) (see, e.g., how the black dash-dotted line penetrates the grey-shaded region after ~ 50 days). We anticipate that other radioactive isotopes (e.g., ^{66}Cu), if they are abundant enough, could increase the radioactive luminosity peak and the exact post-peak decay slope of the light curve. We defer the analysis of this possibility to a more detailed study of the nuclear yields of our models. Nevertheless, for the typical parameters employed to compute the light curve here, the decay of the central engine contribution, rather than the radioactive activity, largely sets the evolution post-peak.

To incorporate the central engine contribution in BH forming models, we assume that the BHs spins down due

to the action of the Blandford-Znajek (BZ) process. A fraction of the spin-down energy boosts a relativistic jet, which penetrates the ejecta and yields a GRB. Another fraction of the energy released, f_{SN} , hits the ejecta and heats it up (in a process analogous to the jet/ejecta interaction shown in Cuesta-Martínez, Aloy & Mimica (2015); Cuesta-Martínez et al. (2015)). We note that the parameter f_{SN} is equivalent to f_{er} in the modeling of the light curves of PMCs. Adapting the results of Nathanail & Contopoulos (2015), the energy released in the SN ejecta due to the spin-down of a BH of mass, M_{bh} , with a magnetic field, B_{bh} , threading its ergosphere is

$$L_{\text{BZ}}(t) = \dot{E}_0 e^{-t/t_{\text{BZ}}}, \quad (16)$$

where, the spin-down e-folding time is

$$t_{\text{BZ}} \equiv \frac{3c}{16G^2 B_{\text{bh}}^2 M_{\text{bh}}} \\ \approx 1.2 \text{ days} \left(\frac{B_{\text{bh}}}{5 \times 10^{13} \text{ G}} \right)^{-2} \left(\frac{M_{\text{bh}}}{2 M_{\odot}} \right)^{-1}. \quad (17)$$

We estimate \dot{E}_0 from the rotational energy of the compact core at $t_{\text{pb}} = t_{\text{f}}$, assuming that a proxy to the BH mass is the mass of the compact remnant at the same time (i.e., $M_{\text{bh}} = M_{\text{r}}(t_{\text{f}})$), and that the typical magnetic field strength in the BH ergosphere is $B_{\text{bh}} \sim B_{\text{surf}}^{\text{pol}}$. Hence, $\dot{E}_0 = f_{\text{SN}} \mathcal{T}_{\text{PNS}}/t_{\text{BZ}}$. As in the PM case, we compute the contribution to the light curve of the BH central engine using

$$L_{\text{bh}}(t) = \frac{e^{-t^2/2t_{\text{r}}^2}}{t_{\text{r}}^2} \int_0^t x e^{x^2/2t_{\text{r}}^2} L_{\text{BZ}}(x) dx. \quad (18)$$

As a reference value, we take $f_{\text{SN}} = 0.1$ (dashed lines in Fig. 14), but we have considered two other values to provide a rough range of uncertainty in the predicted light curve. Precisely, the grey-shaded area in Fig. 14, computed for model A13, is bounded by the cases in which most of the BH spin-down power is transferred to the ejecta ($f_{\text{SN}} = 0.9$; upper boundary of the shaded area) and, by the case in which most of the energy fuels a GRB jet ($f_{\text{SN}} = 0.01$; lower boundary). These two cases may be correlated with the opening angle of the GRB-jet. The smaller the jet opening angle, the most likely it can penetrate the ejecta without heating it up appreciably (cf. Bromberg et al. 2011; Mizuta & Ioka 2013; Aloy et al. 2018). The variation of the free parameter f_{SN} also indirectly accounts for the fact that the time dependence of the BZ process included through (16) is only strictly valid for BHs with moderate or small dimensionless spin (for $a \approx 1$, large deviations in the BZ power can be found; see, e.g., Tchekhovskoy et al. 2010; Mahlmann et al. 2018)). More elaborate models, which are not restricted to a range of BH spins (Okamoto 1992; Lee et al. 2000),² also show a roughly exponential decay of the BZ luminosity. In any case, a temporal decay significantly

² These models neglect the possible evolution of the magnetic flux at the BH horizon induced, e.g., by the accretion of magnetized mass. Indeed, looking at the alternated pattern of magnetized and non-magnetized stellar shells that may be accreted onto the BH, the BZ mechanism may be intermittent and yield variability in the Poynting outflow (Tchekhovskoy & Giannios 2015). But even under these conditions, the BZ process may operate with a relative high efficiency (Mahlmann et al. 2020).

faster than $\sim (1 + t/t_{\text{pm}})^{-2}$ assumed for the PM spin-down. The faster decay of $L_{\text{BZ}}(t)$ compared to $L_{\text{pm}}(t)$ reflects in the faster decay of the light curve past its peak value in potentially collapsar forming models (to which we may refer as proto-collapsars; PCs) compared to PMCs (compare Figs. 13 and 14). Indeed, the decay of the light curve past the peak is so fast that the contribution of the radioactive Ni decay dominates the total luminosity after a time $t_{\text{pb}} \sim 10 t_{\text{pk}}$ (more in the case of models A26 and A30). We critically note that a faster light-curve decline may happen if the breaking index, $m = \tilde{\Omega}\tilde{\Omega}/\tilde{\Omega}^2$ of the PM is significantly smaller than $m = 3$ (which corresponds to the spin-down of a vacuum magnetic dipole). That would make more difficult distinguishing observationally among superluminous events produced by PMCs and PCs on the basis of the decline of the light-curve.

5.3 Extrapolated high energy transient

Considering together the Ni masses, the diagnostic explosion energies listed in Tab. 1 and the extrapolated bolometric light curves of the previous section, we may cautiously suggest the type of high-energy transient that our models may yield. All PMCs display $L_{\text{pk}} \sim 10^{43 \dots 44} \text{ erg s}^{-1}$, i.e., their luminosity is broadly compatible with that of SLSNe. Admittedly, there are (significant) uncertainties in these predictions. The PM breaking index, value of t_{pm} , and the efficiency of conversion of rotational energy into ejecta luminosity are simple estimates. However, we have chosen conservative values of the free model parameters f_{er} and f_{pm} and approximately quantified the uncertainties of the light curve and, at minimum, all PCs would produce rather energetic SNe. For instance, model A17 produces an incipient PM already at $t_{\text{pb}} \sim 3 \text{ s}$ and displays an extremely fast-growing diagnostic explosion energy (Fig. 3). Thus, this model may produce an energetic SN, although in the lower luminosity range of SLSNe ($L_{\text{pk}}^{\text{A17}} \approx 10^{43} \text{ erg s}^{-1}$), with spectral properties compatible with Type Ic SNe, since the amount of Helium in the outer layers of the star is very small. Noteworthy, the kinetic energy of the ejecta in model A17 ($E_{\text{k}}^{\text{A17}} \approx 10^{52} \text{ erg}$) is larger than in any other PMC. The combination of high ejecta kinetic energy and ~ 1 order of magnitude smaller peak luminosity than usual SLSNe is typical of hypernovae, extreme SNe often observed along with GRBs (Moriya et al. 2018). Should an ultrarelativistic outflow form (and produce an associated GRB), it might be launched from the PM some time after the computed evolution in this paper, when the close vicinity of the PNS reduces its density. Model A05 might evolve along similar lines, but with a larger luminosity than model A17, likely qualifying it as a SLSN. Model A08, which also may leave behind an NS rather than a BH, would be characterized by an SLSN ($L_{\text{pk}}^{\text{A08}} \approx 2.6 \times 10^{43} \text{ erg s}^{-1}$). Again, as in the case of model A17, model A08 gathers suitable conditions for the launching of GRB-jet driven by the central PM. Its smaller PNS rotational energy ($\mathcal{T}_{\text{PNS}}^{\text{A08}} \approx 2 \times 10^{52} \text{ erg}$) anticipates a less energetic relativistic transient than in model A17. Thus, for PMCs, the expected observational signature is in line with the predictions of AD18.

Models A13 and A20, for which AD18 predicts a SLSN, along with a PM (or without a central engine in the case

of A13), may indeed produce such a bright SN by the action of its central engine, albeit the later is a BH, instead of a NS. For higher stellar masses, models A26 and A30 display very early peaks ($t_{\text{pk}} < 7$ days), where the luminosity is marginally compatible with that of a SLSN, followed by a plateau that extends for a few months. These models have the compact cores with the largest rotational energy among the CHE models, and among the largest diagnostic explosion energies. These two facts ally to yield the largest ejecta kinetic energies of all PCs ($E_{\text{k}} \sim 10^{52}$ erg). Having peak energies ~ 1 order of magnitude smaller than the rest of the PCs and high kinetic energies, these models may be hypernova candidates (more than SLSNe). Finally, model A39, a borderline case between magneto-rotational and neutrino-driven explosion, features a large peak luminosity ($L_{\text{pk}}^{\text{A39}} \approx 3 \times 10^{43}$ erg s $^{-1}$) in spite of its low central engine initial luminosity ($L_{\text{pm}}^{\text{A39}} \approx 2 \times 10^{45}$ erg s $^{-1}$). The smaller surface average poloidal magnetic field of all the models in Tabs 2 and 3 is the reason for its long decay time, $t_{\text{BZ}}^{\text{A39}} \approx 28$ days, indeed the longest of all CHE models. This decay time is only ~ 4 times smaller than its own effective diffusion time scale t_{r} , compared to, e.g., $t_{\text{r}}/t_{\text{BZ}} \sim 100$ in models A26 and A30, which favours a rather bright transient (Arnett 1982).

Among the BH-forming stars, model 16TI represents the clearest case for a collapsar. While it fails to produce an SN (at least within $t_{\text{pm}} < 6.1$ s), the other stars from this group may produce rather bright explosions, if the effect of the central engine is properly accounted for in our extrapolated light curves (Sect. 5.2). Given their progenitor structure, which enables the possibility of forming an accretion disc, BH forming models could develop a collapsar within a few seconds after t_{f} .

6 CONCLUSIONS

Rotation and magnetic fields are common ingredients to explain some of the most extreme classes of stellar core collapse, viz. SLSNe and GRBs. Single massive stars serving as progenitors of CCSNe may only develop (fast) rotation and (strong enough) magnetic fields under special evolutionary scenarios. AD18 explored such a possibility in stellar-evolution models of stars with enhanced rotational mixing leading to CHE, which ended their hydrostatic burning phases as Wolf-Rayet stars. Based on approximate methods, they found that several of their models with masses between $M_{\text{ZAMS}} = 5 M_{\odot}$ and $M_{\text{ZAMS}} = 39 M_{\odot}$ might explode as SLSNe or as GRBs powered by PMs or collapsars.

We used self-consistent two-dimensional numerical simulations of eight of their progenitors to check these estimates and constrain likely endpoints of the evolution. To this set, we added two rapidly rotating progenitors from Woosley & Heger (2006), model 350C with $M_{\text{ZAMS}} = 35 M_{\odot}$ from our previous studies and model 16TI ($M_{\text{ZAMS}} = 35 M_{\odot}$) that has been employed in various studies of the propagation of jets produced by GRB engines through stellar envelopes. The simulations included special relativistic MHD, an approximately general relativistic gravitational potential, spectral two-moment neutrino transport, and the relevant reactions between neutrinos and matter.

We are able to run the simulations for very long times

(in some cases to $t_{\text{pb}} \gtrsim 6$ s). However, even longer run times would be desired, e.g., to go beyond the formation of a BH, which is currently not feasible with the same approach to the detailed modelling of the microphysics. Furthermore, the assumption of axisymmetry might artificially restrict the dynamics of the stellar cores, in particular when it comes to possible spiral modes of the PNS and the post-shock region (Ott et al. 2005; Blondin & Shaw 2007; Fernández 2010), the amplification of the magnetic field and dynamos (Endeve et al. 2012; Mösta et al. 2015), and the stability of magnetically driven outflows (Mösta et al. (2014); Paper III). Multi-dimensional simulations may also hold the key to removing some of the biggest uncertainties regarding the progenitor, viz. the structure of the magnetic field, in particular in convective layers.

All of our models, save for model 16TI, eventually produce explosions. We find shock revival due to neutrino heating and explosions driven by the magnetorotational mechanism. The latter class of explosion is possible if the PNS and the gain layer possess a strong magnetic field. Whether or not this condition can be fulfilled depends on the distribution of the magnetic field in the progenitor star (in agreement with the findings of Bugli et al. (2020); Paper II). The stellar evolution calculations account for magnetic fields only in radiative layers and neglect them in convective zones. Hence, the gain layer may possess a strong field when a radiative zone is falling through the shock wave, while being only weakly magnetized during the accretion of a convective layer. This connection with the stellar profile makes MHD explosions viable for the stars from AD18 with ZAMS masses of $M_{\text{ZAMS}} = 13, 26,$ and $30 M_{\odot}$, besides our model 350C. In the other models, shock revival is primarily or entirely driven by neutrino heating and non-spherical gas flows.

The large masses of the stellar cores translate in very late explosions in some of the models, in particular at the lower end of the mass range. Once launched, the explosions assume a polar geometry with a more or less pronounced north-south asymmetry. The diagnostic explosion energies are moderate to high with maximum values of up to $E_{\text{exp}} \approx 1.9 \times 10^{51}$ erg, though E_{exp} is still growing by the end of the simulations in most models. If only a fraction of the PNS or BH rotational energy can be tapped and transferred to the SN ejecta on longer timescales than computed here, the implied explosion energies can reach typical hypernova values.

Before and after the explosion, mass accretion increases the masses of the PNS, in some cases driving it above the limit for gravitational stability. Rotation can allow for the PNS to reach a mass close to $M_{\text{PNS}} \approx 3 M_{\odot}$ before collapse. Our simulations end at BH formation or after a few seconds of post-bounce evolution. Hence, our prospects to confirm or disprove the predictions of AD18 regarding the fate of the stars are limited. However, the expected neutron star masses in models that do not form BHs exceed $2 M_{\odot}$, categorising them as massive neutron stars according to Antoniadis et al. (2016).

Although the number of models that we have explored here is very small compared to the large sample of neutrino-driven explosions conducted in Ertl et al. (2016), we find that the two-parameter criterion for the remnant prediction only marginally applies for rotating, magnetized and low-

metallicity stars. BH forming models typically stem from progenitor stars with $\mu_4 > 0.12$, but model A20 challenges this rough division. Instead, a one parameter division according to $\xi_{2.5}$ appears as a simple criterion to distinguish between BH forming ($\xi_{2.5} \geq 0.21$) and PNS forming cases ($\xi_{2.5} < 0.2$). Likewise, a division based upon the rotational energy contained within M_4 allows for a rough classification of the potential remnants: low rotational energies in the pre-collapse stellar matter with $s \leq 4$ ($\leq 1.4 \times 10^{48}$ erg) produce PNSs as compact remnants. We have found a dimensionless parameter, which informs about the explosion type as a function of the magnetic structure in the stellar progenitor, the ratio of the mean poloidal magnetic field length within the inner $2.5 M_\odot$ to the radius of the mass shell $m = 2.5 M_\odot$, $\lambda_{2.5}$. Neutrino-driven explosions result if $\lambda_{2.5} < 0.1$, while magneto-rotational or mixed type explosions occur otherwise. However, we note that the results of this paper apply to axisymmetric models. In 3D the accretion rate onto the PNS may be significantly lowered and the prospects to produce a NSs (on longer terms) increase (Paper III). More systematic studies, including finer grids of models and extended to 3D, will be the subject of future work.

The clearest indication for PM activity can be found in models A17 and A08 where a rapidly rotating and strongly magnetized PNS with too little mass for a BH to form accelerates an MHD wind and injects energy at a high rate into the ejecta. If the model maintained its structure for a substantial time, it would, as suggested by AD18, power a PM-driven GRB. The explosion energies of the two low-mass models, A05 and A08, do not reach particularly high values by the end of the simulation. However, given the rates at which they increase and the strong surface fields of the PNS hint at the possibility of additional magnetorotational energy input on longer timescales. Whether this prospect manifests in the form of an SLSN or a GRB cannot be definitively answered without much longer simulation times.

In all other cases, the PNS collapses to a BH within a few seconds. At their formation, the BHs rotate at only moderate rates with initial spin parameters between $a \approx 0.3$ and $a \gtrsim 0.5$. Mass accretion continues at rates of several $0.01 M_\odot \text{s}^{-1}$. Thus, within several hundreds of seconds, the shells at mass coordinates at $m \approx 3M_\odot$ will fall towards the centre. These shells possess a specific angular momentum around $j \gtrsim 10^{16} \text{cm}^2 \text{s}^{-1}$, which would allow for the collapsar-driven GRBs surmised by AD18. The point at which, according to our simulation, the disk would form, is in good agreement with the estimates shown in Fig. 2, in particular the one marked by the blue asterisk.

The potential for a collapsar-driven GRB is particularly high for model 16TI. Accreting rapidly rotating gas which adds centrifugal support, the PNS grows past the maximum mass for a non-rotating, cold PNS. During an intermittent phase, a shell with super-Keplerian rotation falling onto the PNS forms a geometrically and optically thick torus around the PNS. Inside of the torus, neutrino emission reduces the electron fraction and the entropy. After a few 100 ms, the accretion of gas with lower angular momentum crushes the torus. The rotational profile of the star makes it likely that at a later time, around or briefly after the formation of a BH, a torus of similar characteristics will and allow for collapsar activity.

We have extrapolated our results for models that form PNSs, which we call PMCs following the naming convention in Paper II, assuming that the rotational energy in the compact remnant may be tapped by the PM and contribute to the light curve of the SN explosion at later times. The radioactive decay of Ni produced in our models during the computed post-bounce time also contributes to the light curve. Employing an analytic, one-zone model for the bolometric light curve, we find that our PMCs yield peak luminosities in the range of SLSNe or, at least, bright SNe ($L_{\text{pk}} \gtrsim 10^{43} \text{erg s}^{-1}$). Likewise, we have incorporated the contribution of a BH as a central engine which releases part of its energy into the SN ejecta in PC models. Very luminous SNe result even if the ejecta only receives a small fraction ($f_{\text{SN}} \sim 1\%$) of the rotational energy of the BH. Peak luminosities in the range of SLSNe (say, $L_{\text{pk}} \gtrsim 10^{43 \dots 44} \text{erg s}^{-1}$) are in reach of our models for more efficient energy transfer to the ejecta ($f_{\text{SN}} \sim 10\%$). The central engine contribution dominates the bolometric light curves in all the models analyzed, at least during the first ~ 100 days of the ejecta evolution. BH forming models have a light curve with a steeper (exponential) decay after its peak value, which helps to uncover the radioactive contribution ~ 200 days after the explosion. That change in the slope of the light curve differentiates between a PM central engine and a collapsar. Our axisymmetric models produce insufficient amounts of Ni during the early post-bounce phase to make the radioactive luminosity large enough to be compatible with that of a SLSN. Indeed, the decay of the amount of Ni existing at $t = t_f$ yields peak bolometric luminosities $\lesssim 10^{41} \text{erg s}^{-1}$. Taking aside the contribution of the central engine, the rough estimates of the possible amount of Ni synthesized in our models, yields that magnetorotational explosions lead to brighter SNe than neutrino-driven ones. However, there are other conceivable sources of Ni that our models do not include (e.g., winds emerging from a collapsar accretion disk). Since the luminosity powered by nuclear activity is $L_{\text{nuc}} \propto M_{\text{Ni}}$, we cannot disregard the hypothesis that our stellar progenitors could produce even larger radioactive peak luminosity values. We will explore in a subsequent publication whether 3D versions of our models yield larger Ni masses.

To compute the light curves, we assume that the central engine injects a fraction of its rotational energy into the ejecta on the typical spin-down timescale of a NS (t_{pm}) or of a BH ($\sim t_{\text{BZ}}$). The large difference between the engine injection timescale and the effective photon diffusion time (t_r) does not help to maximize the peak luminosity of the optical transient (Arnett 1982). Nevertheless, the luminosity reaches values within the realm of SLSNe or HNe. The estimation of the spin-down timescale is, however, only approximate. We have computed from our models the values of the instantaneous timescale for the loss of rotational energy of the PNS, $\tau_{\text{rot}} = \mathcal{T}_{\text{PNS}}/|d\mathcal{T}_{\text{PNS}}/dt|$. In line with the results of Paper II, we find that τ_{rot} varies from seconds to hundreds of seconds, thus, $\tau_{\text{rot}} \ll t_{\text{pm}}$. Nevertheless, in our NS forming models, the Kelvin-Helmholtz phase has not finished by the end of the computed time. Hence, we take τ_{rot} as a lower bound of t_{pm} . For BH forming models, our code cannot provide a significant insight on t_{BZ} , since our simulations end by the birth of the BH, but previous analytic work suggest $t_{\text{BZ}} \propto B_{\text{bh}}^{-2} M_{\text{bh}}^{-1}$. That dependence results in $t_{\text{BZ}} \gg t_{\text{pm}}$, which brings the spin-down time of the BH closer

to t_r , boosting the contribution of the central engine to the luminosity in BH forming cases compared to NS forming ones. We have estimated the luminosity without accounting for the contribution of the ejecta/circumstellar medium interaction, something beyond the scope of this paper. But, we envisage that the large energy input coming from the central engine may enhance the aforementioned interaction, especially in BH forming cases. Hence, we deem as not unlikely that our bolometric luminosity estimates are lower bounds of more comprehensive and explicit calculations

Our results confirm that a subset of the massive, rapidly rotating and magnetized stars of AD18 that undergo CHE yield SN explosions with diagnostic explosion energies of the order of that in ordinary CCSNe. Since the stellar progenitors have lost their H envelope and most of the He, the explosion of these models results into Type Ic SNe. The former models are optimally suited to produce the central engine of high energy transients such as GRBs because they meet three conditions. First, the compact remnant left after core bounce possesses a large rotational energy (typically above 10^{52} erg). Second, the stellar progenitor possesses seed magnetic fields that are amplified during collapse. These fields may facilitate the transfer of the compact core rotational energy to the surrounding matter. Third, a fraction of the matter surrounding the central object has a specific angular momentum large enough to support matter against direct collapse, hence enabling the possibility of forming an accretion disc. Whether the central engine is a collapsar or a PM depends on the lifetime of the PNS formed after core collapse.

7 ACKNOWLEDGEMENTS

This work has been supported by the Spanish Ministry of Science, Education and Universities (PGC2018-095984-B-I00) and the Valencian Community (PROMETEUS/2019/071). We furthermore thank for support from the COST Actions PHAROS CA16214 and GWverse CA16104. MO acknowledges support from the European Research Council under grant EUROPIUM-667912, and from the the Deutsche Forschungsgemeinschaft (DFG, German Research Foundation) - Projektnummer 279384907 - SFB 1245 as well as from the Spanish Ministry of Science via the Ramón y Cajal programme (RYC2018-024938-I). The authors thankfully acknowledge the computer resources and the technical support provided by grants AECT-2018-3-0010, AECT-2019-1-0009, AECT-2020-3-0005, and AECT-2021-1-0004 of the Spanish Supercomputing Network on cluster MareNostrum of the Barcelona Supercomputing Centre - Centro Nacional de Supercomputación, on clusters Tirant and Lluisvives of the Servei d'Informàtica of the University of Valencia (financed by the FEDER funds for Scientific Infrastructures; IDIFEDER-2018-063).

DATA AVAILABILITY

The data underlying this article will be shared on reasonable request to the corresponding authors.

REFERENCES

- Aguilera-Dena D. R., Langer N., Antoniadis J., Müller B., 2020, *The Astrophysical Journal*, 901, 114
- Aguilera-Dena D. R., Langer N., Moriya T. J., Schootemeijer A., 2018, *ApJ*, 858, 115
- Aloy M. A., Cuesta-Martínez C., Obergaulinger M., 2018, *Monthly Notices of the Royal Astronomical Society*, 478, 3576
- Aloy M. A., Obergaulinger M., 2021, *Monthly Notices of the Royal Astronomical Society*, 500, 4365
- Antoniadis J., Tauris T. M., Özel F., Barr E., Champion D. J., Freire P. C. C., 2016, *arXiv e-prints*, p. arXiv:1605.01665
- Arnett W. D., 1982, *ApJ*, 253, 785
- Blondin J. M., Shaw S., 2007, *ApJ*, 656, 366
- Bromberg O., Nakar E., Piran T., Sari R., 2011, *ApJ*, 740, 100
- Bucciantini N., Quataert E., Arons J., Metzger B. D., Thompson T. A., 2007, *MNRAS*, 380, 1541
- Bucciantini N., Quataert E., Arons J., Metzger B. D., Thompson T. A., 2008, *MNRAS*, 383, L25
- Bucciantini N., Quataert E., Metzger B. D., Thompson T. A., Arons J., Del Zanna L., 2009, *MNRAS*, 396, 2038
- Bugli M., Guilet J., Obergaulinger M., Cerdá-Durán P., Aloy M. A., 2020, *Monthly Notices of the Royal Astronomical Society*, 492, 58
- Corsi A., Lazzati D., 2021, *New Astronomy Reviews*, 92, 101614
- Cuesta-Martínez C., Aloy M. A., Mimica P., 2015, *MNRAS*, 446, 1716
- Cuesta-Martínez C., Aloy M. A., Mimica P., Thöne C., de Ugarte Postigo A., 2015, *MNRAS*, 446, 1737
- Dado S., Dar A., 2015, *ApJ*, 809, 32
- Dessart L., Hillier D. J., Waldman R., Livne E., Blondin S., 2012, *MNRAS*, 426, L76
- Dessart L., O'Connor E., Ott C. D., 2012, *ApJ*, 754, 76
- Drout M. R., Soderberg A. M., Gal-Yam A., Cenko S. B., Fox D. B., Leonard D. C., Sand D. J., Moon D.-S., Arcavi I., Green Y., 2011, *ApJ*, 741, 97
- Endeve E., Cardall C. Y., Budiardja R. D., Beck S. W., Bejnood A., Toedte R. J., Mezzacappa A., Blondin J. M., 2012, *ApJ*, 751, 26
- Endeve E., Cardall C. Y., Mezzacappa A., 2012, *ArXiv e-prints*
- Ertl T., Janka H.-T., Woosley S. E., Sukhbold T., Ugliano M., 2016, *ApJ*, 818, 124
- Fernández R., 2010, *ApJ*, 725, 1563
- Gal-Yam A., 2012, *Science*, 337, 927
- Gal-Yam A., 2019, *ARA&A*, 57, 305
- Hayakawa T., Maeda K., 2018, *ApJ*, 854, 43
- Heger A., Woosley S. E., Spruit H. C., 2005, *ApJ*, 626, 350
- Inserra C., 2019, *Nature Astronomy*, 3, 697
- Inserra C., Smartt S. J., Jerkstrand A., et al. 2013, *ApJ*, 770, 128
- Iwamoto K., Mazzali P. A., Nomoto K. e. a., 1998, *Nature*, 395, 672
- Janka H.-T., 2012, *Annual Review of Nuclear and Particle Science*, 62, 407
- Just O., Goriely S., Janka H.-T., Nagataki S., Bauswein A., 2021, *arXiv e-prints*, p. arXiv:2102.08387
- Just O., Obergaulinger M., Janka H.-T., 2015, *MNRAS*,

- 453, 3386
- Kasen D., Bildsten L., 2010, *ApJ*, 717, 245
- Kohri K., Narayan R., Piran T., 2005, *ApJ*, 629, 341
- Kumar P., Narayan R., Johnson J. L., 2008, *MNRAS*, 388, 1729
- Lazzati D., Morsony B. J., Begelman M. C., 2009, *The Astrophysical Journal*, 700, L47
- Lazzati D., Morsony B. J., Blackwell C. H., Begelman M. C., 2012, *ApJ*, 750, 68
- Lee H. K., Wijers R. A. M. J., Brown G. E., 2000, *Phys. Rep.*, 325, 83
- Lyman J. D., Bersier D., James P. A., Mazzali P. A., Eldridge J. J., Fraser M., Pian E., 2016, *MNRAS*, 457, 328
- MacFadyen A. I., Woosley S. E., Heger A., 2001, *ApJ*, 550, 410
- Maeda K., Tominaga N., 2009, *MNRAS*, 394, 1317
- Mahlmann J. F., Cerdá-Durán P., Aloy M. A., 2018, *MNRAS*, 477, 3927
- Mahlmann J. F., Levinson A., Aloy M. A., 2020, *MNRAS*, 494, 4203
- Marek A., Dimmelmeier H., Janka H.-T., Müller E., Buras R., 2006, *A&A*, 445, 273
- Metzger B. D., Giannios D., Thompson T. A., Bucciantini N., Quataert E., 2011, *MNRAS*, 413, 2031
- Metzger B. D., Margalit B., Kasen D., Quataert E., 2015, *MNRAS*, 454, 3311
- Mizuta A., Ioka K., 2013, *ApJ*, 777, 162
- Moriya T. J., Sorokina E. I., Chevalier R. A., 2018, *Space Sci. Rev.*, 214, 59
- Mösta P., Ott C. D., Radice D., Roberts L. F., Schnetter E., Haas R., 2015, *Nature*, 528, 376
- Mösta P., Richers S., Ott C. D., Haas R., Piro A. L., Boydston K., Abdikamalov E., Reisswig C., Schnetter E., 2014, *ApJ*, 785, L29
- Müller B., Heger A., Liptai D., Cameron J. B., 2016, *MNRAS*, 460, 742
- Nathanail A., Contopoulos I., 2015, *MNRAS*, 453, L1
- Nathanail A., Strantzalis A., Contopoulos I., 2016, *MNRAS*, 455, 4479
- Nicholl M., Berger E., Margutti R., Blanchard P. K., Milisavljevic D., Challis P., Metzger B. D., Chornock R., 2017, *ApJ*, 835, L8
- Nicholl M., Guillochon J., Berger E., 2017, *ApJ*, 850, 55
- Obergaulinger M., Aloy M. Á., 2017, *MNRAS*, 469, L43
- Obergaulinger M., Aloy M. Á., 2020, *MNRAS*, 492, 4613
- Obergaulinger M., Aloy M. Á., 2021, *MNRAS*, 503, 4942
- Obergaulinger M., Janka H.-T., Aloy M. A., 2014, *MNRAS*, 445, 3169
- O'Connor E., Ott C. D., 2011, *ApJ*, 730, 70
- Okamoto I., 1992, *MNRAS*, 254, 192
- Ott C. D., Ou S., Tohline J. E., Burrows A., 2005, *ApJ*, 625, L119
- Paxton B., Bildsten L., Dotter A., Herwig F., Lesaffre P., Timmes F., 2011, *The Astrophysical Journal Supplement Series*, 192, 3
- Paxton B., Cantiello M., Arras P., Bildsten L., Brown E. F., Dotter A., Mankovich C., Montgomery M. H., Stello D., Timmes F. X., Townsend R., 2013, *The Astrophysical Journal Supplement Series*, 208, 4
- Paxton B., Marchant P., Schwab J., Bauer E. B., Bildsten L., Cantiello M., Dessart L., Farmer R., Hu H., Langer N., Townsend R. H. D., Townsley D. M., Timmes F. X., 2015, *The Astrophysical Journal Supplement Series*, 220, 15
- Paxton B., Schwab J., Bauer E. B., Bildsten L., Blinnikov S., Duffell P., Farmer R., Goldberg J. A., Marchant P., Sorokina E., Thoul A., Townsend R. H. D., Timmes F. X., 2018, *The Astrophysical Journal Supplement Series*, 234, 34
- Rampp M., Janka H.-T., 2002, *A&A*, 396, 361
- Reichert M., Obergaulinger M., Eichler M., Aloy M. Á., Arcones A., 2021, *Monthly Notices of the Royal Astronomical Society*, 501, 5733
- Spruit H. C., 2002, *A&A*, 381, 923
- Steiner A. W., Hempel M., Fischer T., 2013, *ApJ*, 774, 17
- Surman R., McLaughlin G. C., Sabbatino N., 2011, *ApJ*, 743, 155
- Tchekhovskoy A., Giannios D., 2015, *MNRAS*, 447, 327
- Tchekhovskoy A., Narayan R., McKinney J. C., 2010, *ApJ*, 711, 50
- Thompson T. A., Quataert E., Burrows A., 2005, *ApJ*, 620, 861
- Vurm I., Metzger B. D., 2021, *ApJ*, 917, 77
- Woosley S. E., 2010, *ApJ*, 719, L204
- Woosley S. E., Heger A., 2006, *ApJ*, 637, 914
- Woosley S. E., Weaver T. A., 1995, *ApJS*, 101, 181

This paper has been typeset from a \TeX / \LaTeX file prepared by the author.